Solid Earth
Open Access
Discussions

Experimental deformation and recrystallization of olivine – processes and time scales of damage healing during postseismic relaxation at mantle depths

C. A. Trepmann[1], J. Renner[2], and A. Druiventak[2]

[1] Department for Earth and Environmental Sciences, Ludwig-Maximilians-Universität München, Germany
[2] Institute for Geology, Mineralogy, and Geophysics, Ruhr-Universität Bochum, Germany

SED

Deformation and recrystallization of olivine

C. A. Trepmann et al.

Title Page

Abstract	Introduction
Conclusions	References
Tables	Figures

|◄ | ►|
◄ | ►
Back | Close

Full Screen / Esc

Printer-friendly Version

Interactive Discussion

Deformation and recrystallization of olivine

C. A. Trepmann et al.

Abstract

Experiments comprising sequences of deformation (at 300 or 600 °C) and annealing at varying temperature (700 to 1100 °C), time (up to 144 h) and stress (up to 1.5 GPa) were carried out in a Griggs-type apparatus on natural olivine-rich peridotite samples
5 to simulate deformation and recrystallization processes in deep shear zones that reach mantle depth as continuations of seismically active faults. The resulting olivine microfabrics were analysed by polarization and electron microscopy. Core-and-mantle like microstructures are the predominant result of our experiments simulating rapid stress relaxation (without or with minor creep) after a high-stress deformation event: porphy-
10 roclasts ($> 100 \,\mu m$) are surrounded by defect-poor recrystallized grains with a wide range in size (2 to 40 μm). Areas with smaller recrystallized grains ($\leq 10 \,\mu m$) trace former high-strain zones generated during initial high-stress deformation even after annealing at a temperature of 1100 °C for 70 h. A weak crystallographic preferred orientation (CPO) of recrystallized olivine grains is related to the orientation of the host
15 crystals but appears unrelated to the strain field. Based on these findings, we propose that olivine microstructures in natural shear-zone peridotites with a large range in recrystallized grain size, localized fine-grained zones, and a weak CPO not related to the strain field are diagnostic for a sequence of high-stress deformation followed by recrystallization at low stresses, as to be expected in areas of seismic activity. We extended
20 the classic Avrami-kinetics equation by accounting for time-dependent growth kinetics and constrained the involved parameters relying on our results and previously reported kinetics parameters. Extrapolation to natural conditions suggests that the observed characteristic microstructure may develop within as little as tens of years and less than ten thousands of years. These recrystallization microstructures have a great diagnostic
25 potential for past seismic activity because they are expected to be stable over geological time scales, since driving forces for further modification are not sufficient to erase the characteristic heterogeneities.

Title Page

Abstract | Introduction

Conclusions | References

Tables | Figures

Back | Close

Full Screen / Esc

Printer-friendly Version

Interactive Discussion

1 Introduction

In the tectonic environment of subduction zones, shear zones can reach down to mantle depth as continuation of seismically active fault zones, as for example observed for the Sumatra earthquake in 2004 that caused the infamous tsunami (Singh et al., 2008;
5   Dessa et al., 2009). The macro-scale time-dependent rheology of such shear zones is controlled by nano- to micro-scale deformation and recrystallization processes in the affected upper mantle rocks (i.e. peridotites). What are these processes and what are their characteristic time scales for damage healing? These questions can be addressed by experimentally studying deformation and recrystallization processes during
10   characteristic stress sequences. Large earthquakes generate short-term high strain rates and stresses at depth below the seismogenic zone and below the long-term lithospheric brittle-viscous transition, causing transiently brittle mechanisms at depth where at lower stress the material shows ductile behaviour (e.g. Sibson, 1980; Schloz, 2002; Ellis and Stöckhert, 2004; Nüchter and Ellis, 2010). This temporal change in rheology
15   is reflected by:

1. seismological observations: maximum hypocenter depths are initially larger than that of the preceding background seismicity and then decrease gradually with time to the background level (e.g. Ben-Zion and Lyakhovsky, 2006; Ben-Zion, 2008). Aftershocks following large earthquakes occur transiently at larger depth than the
20   main event (e.g. Schaff et al., 2002; Rolandone et al., 2004), and

2. the microstructural record of deformation and recrystallization from exhumed metamorphic rocks (e.g. Küster and Stöckhert, 1999; Trepmann and Stöckhert, 2001, 2002, 2003; Nüchter and Stöckhert, 2007; Birtel and Stöckhert, 2008; Matysiak et al., 2012).

25   Despite the important influence of rapidly changing stresses and strain rates on deformation and recrystallization, these processes are commonly discussed from a perspective of long-lasting constant stress and strain-rate conditions (Platt and Behr, 2011a,

b). The focus on deformation and recrystallization at long-lasting stationary conditions owes partly to the lack of diagnostic features in the geological record that can be used to assess whether recrystallization occurs continuously together with deformation (dynamic recrystallization) at relatively constant stresses or subsequently to deformation
5   at high stress when stresses are low and insufficient to maintain inelastic deformation (static recrystallization). Microstructures formed at rapidly evolving conditions during coseismic loading and postseismic relaxation superimpose each other and a prolonged thermal history of exhumed rocks causes a modification of the earlier features. Therefore, non-steady state experiments at successively different stress conditions are
10 needed to identify characteristic overprinting microfabrics and the relevant time scales of their evolution.

Olivine in peridotites experimentally deformed at low temperatures and high stresses reveals specific microstructures (Druiventak et al., 2011) that are modified by recovery and recrystallization to core-and-mantle like microstructures during annealing at
15 quasi-isostatic conditions (Druiventak et al., 2012). The experimentally derived core-and-mantle like microstructures are strikingly similar to those from shear zone peridotites often interpreted to be formed by continuous dynamic recrystallization during dislocation creep at relatively constant stresses.

The primary objectives of this experimental study are documenting the microfabric
20 evolution and constraining the kinetics parameters of static recrystallization of olivine after high-stress deformation. For this end, we carried out deformation and isostatic annealing ("kick and cook") experiments at various temperatures and times, simulating quasi-instantaneous stress relaxation and a subsequent prolonged isothermal low-stress event. We aim at establishing relations between deformation conditions, anneal-
25 ing temperature, and annealing time on the one hand and area percentage, grain size, and crystallographic characteristics of recrystallized olivine on the other. In addition, we want to find out to what extent complex stress histories as likely occurring in natural situations affect the characteristic microfabrics and how the modified microstructure affects rock strength. We therefore (a) simulate creep at low stresses during recrystallization

("kick and creep") and (b) repeat deformation after a first deformation and isostatic annealing ("kick-cook-kick"). The microstructural findings from our experiments and the inferred kinetics parameters are used to discuss the time-dependent rheology and damage healing processes in shear zones that occur at mantle depths as continuations of seismically active faults.

2   Characteristics of the experimental approach

2.1   Experimental protocol

The Griggs-type apparatus, its sample assembly, and the sample material, a coarse-grained (grain size 0.2 to 1 mm) peridotite (up to 90 % olivine) from the Almklovdalen complex, Norway, have previously been described in detail (Druiventak et al., 2011, 2012). In this study, five suites of experiments were carried out with varying sequences of deformation and annealing.

1. To simulate instantaneous stress relaxation after high-stress deformation, samples were deformed at temperatures of 300 and 600 °C, at a confining pressure of 1 GPa. The strain rates varied between 3×10^{-5} and $8 \times 10^{-5}\,\text{s}^{-1}$ (Table 1). After deformation, the axial piston was retracted and samples were heated at a constant rate of $5\,°\text{C}\,\text{min}^{-1}$ to temperatures of 700 to 1100 °C. To avoid melting of the confining medium, the confining pressure was simultaneously increased at a constant rate to GPa and these conditions were held for ca. 16, 70 or 144 h. These "kick and cook" experiments follow the original set up for studying microstructure development during coseismic loading and postseismic relaxation in quartz-rich lithologies (Trepmann et al., 2007), later applied to natural peridotites by Druiventak et al. (2012).

2. Two reference annealing experiments without preceding deformation ("cook", Table 1) were performed at a temperature of 1000 °C, a confining pressure of 2 GPa,

467

and a duration of ca. 70 h. One experiment was performed in the Griggs-type apparatus (B9026) and one in a standard piston cylinder apparatus (B9032) (Renner et al., 1997).

3. To simulate creep during the period of stress relaxation three experiments were conducted with the first deformation stage as in (1) and continued deformation during heating and annealing at 1000 °C and 2 GPa for ca. 70 h (Table 2). In these "kick and creep" experiments, the piston was not retracted before heating and annealing. During one experiment (B9037) the axial piston remained at its final position of the first deformation step. During heating stress relaxation may have been partly counteracted by thermal expansion of the piston and the sample. Stress relaxation then dominated during isothermal annealing. The axial piston was advanced from its end position with a velocity of 0.15 mm h^{-1} during experiment B9039 for ca. 0.7 h during heating from 600 to 850 °C. In experiment B9038 the piston was advanced with a velocity of 0.75 mm h^{-1} during the entire heating period lasting for ca. 2 h.

4. To simulate a repeated seismic event, "kick-cook-kick" experiments were carried out comprising deformation and subsequent quasi-isostatic annealing as in (1) and finally a second deformation step at 1 GPa and 300 °C (B9040) or 600 °C (B9014), experiment B9015 was deformed during both high-stress stages at 600 °C and 2 GPa (Table 2).

5. One reference experiment ("cook-and-kick" B9044) was carried out without the first deformation but starting with isostatic annealing at 1000 °C for 70 h followed by deformation at 600 °C and 1 GPa confining pressure (Table 2).

2.2 Analytical techniques

The olivine microfabrics of tested samples were analysed by optical microscopy, scanning electron microscopy (SEM) including electron back scatter diffraction (EBSD), and

transmission electron microscopy (TEM). Polarization microscopy was performed on polished thin sections (30 μm thick). A SEM (LEO 1530) instrument equipped with field emission gun and forescatter detector was used for automated EBSD measurements with a step size of 0.7 to 1 μm. For the TEM analysis, a Phillips EM301 microscope operating at 100 kV was used. The TEM foils (100 to 200 nm thick) were prepared by the focused ion beam (FIB) technique.

The area covered by recrystallized grains, further referred to as recrystallization area, was mapped for all samples relying on images gained by optical microscopy (see Tables 1 and 2). EBSD measurements provided information on the spatial distribution of the crystallographic orientation of grains in recrystallized areas. Since recrystallized grains were generally too small to be analysed by optical microscopy in 30 μm thick sections, EBSD maps were also used for grain size analysis, despite the general difficulty to distinguish between mis-indexing and small real grains. Grain sizes were estimated using a threshold of a relative crystallographic misorientation angle of 10° to formally distinguish between subgrains and grains.

The quoted recrystallized grain size represents the diameter of a circle of equivalent area. Given the applied step size of 0.7 to 1 μm for automatic EBSD measurements, grains with a diameter below 2 μm were neglected. The average grain diameter is given as the expectation value of the associated grain size distribution. Variability in grain size within a sample is represented by the standard deviation in grain size (see Tables 1 and 2). Typically, grain size distributions show the maximum for the lowest grain size bin (< 5 μm), then grain size frequencies rapidly decrease to zero. Maximum recrystallized grain size is reported as the diameter of the last bin class with a non-zero frequency. Clearly, the absolute values for grain size determination are strongly dependent on the processing routine of the EBSD data. Here, all measurements were processed by strictly the same routine to ensure that the data are significant for a comparison of the results from the various experiments employing different deformation and annealing conditions.

3 Results – mechanical data

Maximum differential stress, $\Delta\sigma_{max}$, and maximum strain, ε_{max}, (sum of elastic and inelastic strain) reached during deformation were derived from stress-strain curves after friction correction (Rybacki et al., 1998). The maximum differential stress ranged be-
5   tween 1 and 1.5 GPa during the initial deformation stage (Table 1). A weak temperature dependence of strength can be noticed from mean values of differential stress at 10 % strain (Fig. 1). On average, samples deformed at 300 °C show a higher strength than those deformed at 600 °C (see also Druiventak et al., 2011).

The stress-strain curves yield maximum strain between 14 and 28 %, correlating
10   well with the permanent shortening ε_{total} between 5 and 33 % as determined from calliper measurements on recovered samples after the experiments (Table 1). Shortening of samples in the reference annealing experiments without preceding deformation ("cook") amounts to 3 % for the sample tested in the Griggs-type apparatus and 1 % for the sample tested in the piston-cylinder apparatus (Table 1).

15   Most of the stress-strain curves show systematic softening with increasing strain. Due to the inherent uncertainty of the friction corrections in solid-media apparatus (e.g. Rybacki et al., 1998; Holyoke and Kronenberg, 2010) it is possible that the curves indicating softening do not all reflect actual material behaviour. Yet, the cases for which stress decreases prominently with increasing strain (Fig. 1) correlate with the obser-
20   vation of local shear zones in the deformed samples (Fig. 2). The slight variations in applied strain rates do not affect strength (Table 1).

Strains accumulated during the "creep" stage in "kick and creep" experiments, ε_{creep}, in which the piston was slowly advanced or remained at its final position of the deformation stage during the annealing, range from 10 to 29 %, as calculated from the
25   difference between total strain determined from the shortening of the sample after the experiment and the strain derived from the stress-strain curves of the low-temperature deformation ("kick" stage) (Table 2). These strains correspond to approximate strain rates between 10^{-6} and 10^{-7} s^{-1} gained from simply dividing accumulated strain by

Title Page

Abstract	Introduction
Conclusions	References
Tables	Figures

|◄   ►|

◄   ►

| Back | Close |

Full Screen / Esc

Printer-friendly Version

Interactive Discussion

the duration of the high-temperature stage (Table 2). Differential stress at this stage is estimated to be somewhat below 0.5 GPa using the flow law for dislocation creep of olivine after Chopra and Paterson (1981) and assuming that at this stage olivine deforms by dislocation creep at the given temperature of 1000 °C and the inferred strain
5 rates. Clearly, differential stress and strain rate are not constant during the creep stage.

Strain during the second low-temperature deformation after isostatic annealing can be estimated in two ways: (1) taking the difference between the total strain ε_{tot} representing the permanent shortening of the sample and the strain ε_{max1} derived from the stress-strain curves of the first deformation leads to 11 to 20 %; (2) directly analyzing
10 the "second" stress-strain curve gives comparable strains ε_{max2} of 9 to 16 % (Table 2). Maximum differential stresses during this second deformation stage exceed those observed during the first. The friction characteristics changed relative to the first deformation stage when the experiment was cooled down to the temperatures of the second deformation stage (300, 600 °C) after extended high-temperature annealing rendering
15 the quoted stresses of the second stage more uncertain. A reduction in strength from the first to the second deformation stage can however be excluded. The same applies to the reference experiment without a first deformation stage ("cook-kick").

4 Results – olivine microfabric analysis

Microstructures resulting from the high-stress deformation ("kick") are described in
20 detail by Druiventak et al. (2011). In this study, the focus is on the evolution of the olivine microfabric during subsequent annealing at varying temperatures, durations, and stresses. As the high-stress deformation determines the olivine microfabric evolution during subsequent annealing, the main characteristics ought to be summarised here. The olivine grains with an original diameter of 0.2 to 1 mm show intragranular frac-
25 tures, some of which may be pre-existent features (Fig. 2a). Localized, highly damaged zones of a few tens to 100 μm in width are characterized by systems of intergranular fractures (Fig. 2b). The fragments in these highly damaged zones show strong patchy

undulatory extinction associated with high relative misorientation angles as evidenced by EBSD and with a high density of dislocations, cellular domains, and voids as found by TEM (see also Druiventak et al., 2011, 2012). The highly damaged zones constitute an area percentage of 5 to 7 %.

In samples from the reference annealing experiments at 1000 °C for 70 h without preceding experimental deformation (B9026, B9036), small grains with a diameter of 4 to 5 µm occur locally along boundaries and former cracks of the coarse-grained original olivine crystals. These small grains are referred to as recrystallized grains. An area of about 1 to 3 % of the reference samples is covered by the recrystallized grains.

4.1 Microfabrics after deformation and annealing ("kick and cook")

4.1.1 Types of grains

In the deformed and then annealed samples, the differentiation between original host grains and recrystallized grains, as described above in the reference samples (B9026, B9036), is not as straight forward, given the locally strong grain size reduction by brittle and glide-controlled crystal-plastic deformation, especially in the highly damaged zones (Fig. 3). Different types of grains are differentiated on the basis of the microstructures of samples deformed at 300 or 600 °C and annealed at 700 °C. In these samples that experience annealing at the lowest temperature, optically, a marked modification is not resolved compared to the microstructures observed immediately after deformation (Fig. 4). In TEM, the highly damaged zones represented by a high density of dislocations that occur in tangles containing dislocation-poor domains is still present after 144 h of annealing, irrespective whether initial deformation occurred at 600 °C (Fig. 4b) or at 300 °C (Fig. 4d). The combination of EBSD maps and TEM observations (Fig. 4), however, reveals that recrystallized grains occur locally after annealing for 144 h even at this lowest annealing temperature. At this stage of incipient recrystallisation we can subdivide two different types of recrystallized grains:

1. Almost defect free tiny (< 1 µm) crystalline volumes occur within crystalline material of very high defect density composing the highly damaged zones originating from the high-stress deformation stage (Fig. 4b, d). This type of recrystallized grains is subsequently referred to as "new grains". Voids occur along the boundaries of new grains but also within the matrix of high defect density.

2. Grains of a few micrometers or a few tens of micrometers with smoothly curved grain boundaries and an inherited defect density are interpreted to originate from small fragments of original grains whose boundaries lost their angularity driven by curvature reduction during incipient heat treatment (Fig. 4c). These grains are referred to as "recrystallized host fragments". Voids of 1 to 2 µm in diameter are present at three-grain junctions and smaller voids between two grains. The differentiation between "recrystallized host fragment" and "new grains" thus reflects both, the variance in defect density and grain size. A distinction between "recrystallized host fragment" and "porphyroclasts" is established solely on the basis of size: porphyroclasts are defined by a long axis of grains > 100 µm, i.e. > 10 to 50 % of the original grain size of the natural peridotites.

Optically, new grains and recrystallized host fragments cannot be distinguished, especially in samples that experienced low annealing temperature for short duration, and are summarized as "recrystallized grains" when describing bulk properties. A differentiation between new grains and recrystallized host fragments at SEM and TEM scale is obvious and required when discussing grain boundary migration processes during growth. Grains with inherited dislocation density (i.e. recrystallized host fragments plus porphyroclasts) are summarized as deformed grains.

4.1.2 Development of recrystallized area and grain size during isostatic annealing

A dependence of recrystallized grain size and area on deformation temperature is not obvious from our data (Fig. 5a, b) but a strong dependence on annealing temperature

Deformation and recrystallization of olivine

C. A. Trepmann et al.

and time (Figs. 5c, d, 6). Recrystallization area (up to 30 %) and average diameter of recrystallized grains (3 to 10 μm) increase with annealing temperature and time (see also Table 1). Recrystallized grains occur in zones between porphyroclasts and in intragranular zones. Most prominently, they follow the original highly damaged zones

⁵ generated during the high-stress deformation stage (Fig. 3). The size of recrystallized grains varies strongly within one sample, as reflected by the high standard deviation (Table 1). The variability slightly increases with increasing annealing temperature and annealing time not only in absolute values but also relative to the expectation values (Fig. 5a).

¹⁰ Generally, less than a few percent of the area of a sample are recrystallized after annealing at temperatures of $\leq 900\,^{\circ}$C. The microstructural observations indicate that the highly damaged zones formed during deformation are completely replaced by recrystallized grains after annealing for 70 h at 900 °C. At higher temperatures, recrystallization affects an area beyond the optically-defined highly damaged zones. Generally, the

¹⁵ striking microstructure of porphyroclasts surrounded by recrystallized grains observed after annealing at temperatures of $\geq 900\,^{\circ}$C is similar to what is commonly addressed as core-and-mantle structure (e.g. Fitz Gerald and Stünitz, 1993; Passchier and Trouw, 2008; Stipp and Kunze, 2008).

New grains and recrystallized host fragments differ prominently also after anneal-

²⁰ ing at high temperature for a long time: in samples annealed at 1000 °C for 144 h, EBSD maps reveal isometric new grains that do not show any intracrystalline deformation features and that have smoothly curved high-angle grain boundaries (Fig. 7). Recrystallized host fragments, in contrast are characterised optically and in EBSD maps by varying crystallographic orientation within one grain (i.e. undulatory extinction), the

²⁵ presence of low-angle grain boundaries, sutured high-angle grain boundaries and irregular grain shapes (Fig. 7). Even after isostatic annealing at 1100 °C for 69 h, the recrystallized host fragments show mostly concave and sutured boundaries (labelled "h" in Fig. 8a) whereas new grains exhibit isometric shape with curved convex boundaries. Triple junctions of new grains are characterized by angles of about 120˚ (yellow

arrow in Fig. 8a), which is not the case for the recrystallized host fragments (red arrow in Fig. 8a). The new grains typically retain a small diameter of $< 10\,\mu m$ and occur concentrated in zones that are interpreted to follow former highly damaged zones (Fig. 8a). The exact differentiation between recrystallized host fragments and porphyroclasts becomes increasingly ambiguous, as the grain size of porphyroclasts shrinks as they are replaced by the growing recrystallized grains (Fig. 8a). Despite this ambiguity in detail, however, it can be safely stated that an area $> 70\,\%$ of the sample is covered by porphyroclasts (host fragments $> 100\,\mu m$) even at the highest annealing temperature of $1100\,^{\circ}C$ (B9036, Fig. 8).

In TEM, the different characteristics of recrystallized host fragments and new grains are apparent by their respective intracrystalline defects: recrystallized host fragments show low-angle grain boundaries arranged in short, commonly subparallel sets and a low to moderately high ($< 10^{13}\,m^{-2}$) dislocation density (Figs. 8b, c, 9). New grains are free of low-angle grain boundaries and contain almost no dislocations (Figs. 8b, c, 9a–c, f). The boundaries between two new grains (Fig. 9a, b) as well as the boundaries between new grains and recrystallized host fragments (Figs. 9c, f, 10b, c) are partly decorated by tiny voids. Either type of boundary, between new grains and host grains or between two new grains, is smoothly curved.

4.1.3 CPO of recrystallized grains

New grains that occur in intragranular zones show a relative misorientation angle of generally higher than 30° compared to their host and no systematic orientation relationship to the host or the shortening direction (Fig. 10a, b). In contrast, larger aggregates of new grains and recrystallized host fragments (Fig. 10c) and consequently the bulk CPO of recrystallized olivine grains (Fig. 11) show a marked imprint of the crystallographic orientation of the host crystal rather than to the shortening direction. For low annealing temperatures (700 and $800\,^{\circ}C$), the orientation of recrystallized grains is strongly controlled by the host; with increasing temperature the scatter in crystallographic orientation increases (Fig. 11).

4.2 Microfabrics after deformation and a subsequent low-stress, high-temperature stage ("kick and creep")

The main characteristics of the microfabrics found after high-stress deformation and a high-temperature creep stage at 1000 °C for 70 h and stresses about 3 times lower
5 than those during the "kick" stage (i.e. 0.5 GPa) are comparable to those of samples that experienced isostatic annealing at the same temperature for the same duration. Core-and-mantle like structures are found (Fig. 12a, b); the average diameter of recrystallized grains is about 6 µm (see Tables 1 and 2); the observed CPO patterns are variable with strong scatter in orientations and unsystematic correlation with the host
10 orientation (Fig. 11). Yet, an increase in recrystallized area to 24 to 26 % is observed for samples after "kick and creep" experiments compared to only 7 to 13 % in the isostatically annealed samples at otherwise comparable conditions.

4.3 Microfabrics after deformation, annealing and renewed low-temperature deformation ("kick-cook-kick")

15 In samples that experienced a second high-stress, low-temperature deformation stage after an initial high-stress deformation and isostatic annealing ("kick-cook-kick"), elongate remnants of bent original grains with internal misorientation are observed in direct contact to zones of recrystallized grains (Fig. 12c, d). Strain accumulated during the second high-stress deformation therefore appears to localize in the porphyroclasts
20 rather than in the fine-grained recrystallized zones. Microstructures from the "cook and kick" reference experiment (B9044, annealed at 1000 °C for 70 h, deformed at 600 °C) show some isometric recrystallized grains along boundaries of large original grains comparable to the "cook" reference samples B9026 and B9032 and otherwise deformation microstructures (fractured original grains and highly damaged zones) comparing
25 well to the "kick" experiments.

Title Page

Abstract | Introduction

Conclusions | References

Tables | Figures

◄ | ►

◄ | ►

Back | Close

Full Screen / Esc

Printer-friendly Version

Interactive Discussion

5 Discussion

The recrystallization features observed in our reference samples annealed without pre-ceding experimental deformation are interpreted to be a result of the rocks natural strain history rather than non-hydrostatic stress states during the experiments. The ob-served recrystallized grains supposedly develop by grain boundary migration of small crystalline, relatively defect-free volumes surrounded by naturally strained areas of the peridotites, i.e. along grain boundaries or pre-existent fractures. Yet, the recrystallized area observed after the hydrostatic reference "cook" experiments in the Griggs appa-ratus (B9026) and the piston cylinder apparatus (B9032) differs. The difference may be a result of sample to sample variability but may also indicate a poorer realization of hydrostatic conditions in the Griggs apparatus. If the latter is true, the microstructural observations of all experiments may be slightly biased by a recrystallization fraction of up to 3 % not necessarily directly correlated with the imposed experimental conditions. The sites most prone to recrystallization due to an inherited natural deformation his-tory may, however, also accommodate the experimental deformation. If so, the recrys-tallized area observed during the reference experiments does not constitute a bias to our observations. The extent of these recrystallization phenomena is so restricted that their occurrence does not significantly affect our discussion. Furthermore, the "starting material" in nature will typically also have some strain energy stored from preceding events when a high-stress event takes place.

In the following, we firstly discuss the recrystallization processes for the two identified types of recrystallized grains distinguished from our "kick and cook" experiments, then specifically address the quantitative grain size evolution during isostatic annealing, the kinetics of static recrystallization and finally the implications of our study with regards to extrapolation to natural conditions and recognition of diagnostic microstructures in natural samples. We conclude with a brief note on reloading scenarios.

5.1 Evolution of the two different types of recrystallized grains

The "kick" stage at 300 and 600 °C leads to a transient marked grain size reduction by fracturing together with glide-controlled crystal-plastic deformation but evidence for recrystallization is lacking (see also, Druiventak et al., 2011, 2012). Thus, the recrys-
⁵ tallised grains observed after isostatic annealing develop exclusively by static recrystallisation after deformation. The increase in recrystallized grain size with increasing annealing temperature and duration indicate that "nucleation and growth" processes are active to different degrees when recrystallization proceeds during heating and isostatic annealing with and without superposed creep.
¹⁰ Based on the microstructural observations we distinguished two fundamentally different types of recrystallized grains:

1. The first type referred to as "new grains" formed within highly damaged zones (Figs. 8, 10a). We suppose that their precursors differentiate into

   – crystallites: tiny dislocation-free volumes ($< 2\,\mu m$) formed by comminution,

¹⁵   – cell structures: dislocation-free domains surrounded by dislocation tangles, formed by dislocation glide during high-stress deformation.

   At an early stage of annealing at 700 °C (Fig. 4b, d), these grains are represented by the defect-free domains with a diameter $< 2\,\mu m$, both are surrounded by crystalline material containing a high density tangled dislocation. Since annealing
²⁰ proceeds at isostatic conditions new grains do not develop internal deformation features. The crystallographic orientation of new grains appears nearly random and only weakly controlled by the crystallographic orientation of the host crystal (Fig. 10). Their orientation does not show a relation to the stress orientation of the initial deformation.

²⁵ Both, crystallites and cell structures, are formed during deformation and thermally activated nucleation like in displacive phase transformations probably does

Title Page

Abstract | Introduction

Conclusions | References

Tables | Figures

◄ | ►

◄ | ►

Back | Close

Full Screen / Esc

Printer-friendly Version

Interactive Discussion

not apply to static recrystallisation. Nevertheless, some thermal affects may contribute, such as cell-wall migration and rounding of granular fragments. However, the similarity between quantitative microstructural characteristics found for annealing after deformation at 300 °C and 600 °C (Fig. 4) suggests these contributions to be small. Thus, "nucleation" does not occur in the classical sense used for phase transformations but rather constitutes a process of "initiation", during which small crystalline volumes of low internal strain energy grow on the expense of deformed material (e.g. Humphreys and Hatherly, 2004). We still use the term "nucleation" here, given the small size of the precursors ("seeds" or "nuclei") embedded in the highly disordered crystal lattice. The formation of these new grains is different from subgrain rotation recrystallization (i.e. polygonisation) or bulging recrystallization (e.g. Drury and Urai, 1990; Shimizu, 1998; Stipp and Kunze, 2008; Platt and Behr, 2011), for which the larger precursors inherit the crystallographic orientation of the host and which are processes that require ongoing deformation with continuous dislocation production, i.e. dynamic recrystallization. Similar observations of high misorientation between new grains and weak to absent orientation control by the host crystals developed from sites, where the crystal lattice is highly disordered (Fig. 4b, d), has also observed for example in quartz (Trepmann et al., 2007) and feldspar (Stünitz et al., 2003).

2. The second type of recrystallized grains differ mainly from new grains by (a) the inherited defects from the initial deformation stage, (b) their larger size (up to a few tens of µm, Fig. 4c) compared to that of the crystallites (< 2 µm) from which the new grains develop, and (c) the separation to other fragments by high-angle grain boundaries (Fig. 4c). After isostatic annealing the recrystallized host fragments contain low-angle grain boundaries and show sutured grain boundaries (Figs. 4c, 7, 8). Fragments that experienced little rigid body rotation during comminution results in an orientation controlled by the host crystal.

Title Page

Abstract | Introduction

Conclusions | References

Tables | Figures

|◄ | ►|

◄ | ►

Back | Close

Full Screen / Esc

Printer-friendly Version

Interactive Discussion

The weak CPO (Fig. 11) in the bulk areas of recrystallized grains (new grains plus recrystallized host fragments) is not interpretable in terms of intracrystalline glide systems requiring dynamic recrystallization resulting in recrystallized grains preferentially oriented with the active glide direction parallel to the stretching lineation and the glide
⁵ plane in the foliation plane.

5.2 Grain size evolution during isostatic annealing

Growth of recrystallized grains occurs dominantly during isostatic annealing. Given the short time of heating from 600 °C to the final annealing temperature (max. 2.3 h) in comparison to the extended duration of annealing (16 to 144 h), the contribution of
¹⁰ growth during the heating phase can be neglected. Growth of defect-free new grains surrounded by crystalline material with a high defect density is initially driven by the reduction in strain and surface energies. Boundaries between defect-free new grains are solely controlled by interfacial free energy, whereas other grain boundaries (between deformed grains and between new grains and deformed grains) are continuously mi-
¹⁵ grating driven by gradients in the defect density.

A positive correlation between the final grain size attained during static recrystallisation and annealing temperature as observed here (Fig. 5b, c, Table 1) has also previously been reported, as has a negative correlation between resulting grain size and accumulated bulk strain during the preceding deformation (e.g. Fig. 4.16 in Nicolas and
²⁰ Poirier, 1976; Humphreys and Hatherly, 2004). Strain affects the number of nucleation sites (e.g. Humphreys and Hatherly, 2004) as much as it affects the degree and spacial extent of crystal damage. In addition, the defect content of the deformed material affects the driving force for growth and potentially also the grain boundary mobility. Spacial heterogeneity in local strain is characteristic for deformation in the regime of
²⁵ low-temperature plasticity associated with fracturing dominant in the "kick" steps of the experiments (Druiventak et al., 2011). Thus, even in a single sample the variability of local strain and associated inelastic deformation causes variations in the recrystallisation characteristics.

The observed range in grain sizes in samples from experiments after annealing at high temperatures ($\geq 900\,°C$) and long annealing times ($\geq 69\,h$) can be explained by a negative correlation between grain size and strain (Figs. 8a, 10a, Table 1). The fine-grained ($< 10\,\mu m$) zones represent sites of high nucleus density, i.e. former highly damaged zones, where many nuclei are created and they mutually hinder each other in their growth due to impingement. In contrast, at some distance of the highly damaged zones fewer and larger recrystallised grains (up to $40\,\mu m$) occur (Fig. 10a), likely due to a lower nucleus density for new grains and/or predominant occurrence of recrystallized host fragments over new grains. Furthermore, for the new grains that are almost free of defects on the one hand and the recrystallized host fragments that inherit the deformed microstructure on the other, variations in the driving force for growth during isostatic annealing have to be considered (see for example Hackl and Renner, 2013, for an analytic expression of the dependence of a grain's size evolution on the relation between its energy state and that of its environment).

The driving force for growth of recrystallized grains, i.e. the difference in their free energy and that of their environment, is here simply associated with two defect concentrations, the density of interfaces and dislocations,

$$\Delta G = \Delta G_\gamma + \Delta G_\rho = \gamma \left(\frac{1}{d_{\text{def}}} - \frac{1}{d_{\text{rec}}} \right) + \mu b^2 \left(\rho_{\text{def}} - \rho_{\text{rec}} \right). \tag{1}$$

In our samples, the free energy of new grains is dominated by their interfacial energy while that of deformed grains is dominated by strain energy represented by dislocation density (Fig. 13a). We therefore approximate the driving force by $\Delta G \simeq -\gamma/d_{\text{rec}} + \mu b^2 \rho_{\text{def}}$ yielding a condition for the minimum size of a new grain to grow in expense of the deformed grains, $d_{\text{rec,min}} = \gamma/\mu b^2 \rho_{\text{def}}$.

A quantitative analysis of the critical size for a recrystallisation nucleus in olivine aggregates yields between 10 and a $100\,nm$ in volumes with a dislocation density of $\sim 10^{15}\,m^{-2}$ (within half an order of magnitude) assuming $\gamma \sim 1\,J\,m^{-2}$ (see Table 3a). The minimum size directly scales with interfacial energy, thus the minimum size for subgrain

Deformation and recrystallization of olivine

C. A. Trepmann et al.

Title Page

Abstract	Introduction
Conclusions	References
Tables	Figures

|◀ | ▶|

◀ | ▶

| Back | Close |

Full Screen / Esc

Printer-friendly Version

Interactive Discussion

nuclei may be even smaller than the value above due to the order of magnitude reduction in their interfacial energy relative to the value of large-angle grain boundary energy used here. Once a material volume is solely composed of new grains (e.g. complete replacement of highly damaged zones) normal grain growth sets in controlled by a driving force that is dominated by the relative relation between the curvature of the grain boundaries (e.g. Atkinson, 1988; Evans et al., 2001).

At all stages, grain boundary migration may be affected by pinning due to voids present on the grain boundaries (Fig. 9) that are relics of low-temperature plasticity associated with brittle deformation preceding the annealing. In contrast, strain-induced migration of boundaries between defect-free new grains and recrystallized host fragments or porphyroclasts with inherited defect-density can further proceed due to gradients in stored strain energy. The observation that the recrystallized area exceeds the area of original highly damaged zones after annealing at high temperature ($\geq 900\,°C$) and time ($\geq 69\,h$) may indeed be explained by ongoing strain-induced grain boundary migration after the complete replacement of the highly damaged zones.

Our data set is clearly affected by the lower limit in resolution of the EBSD-based grain size analysis. Yet, the size of recrystallized grains is sufficiently large for growth to be resolved for annealing temperatures exceeding $\geq 900\,°C$. Grain growth is traditionally modeled by laws of the form

$$d_{(t)}^m - d_0^m = k_{gg}t, \tag{2}$$

where $k_{gg} = k_{gg,0}\exp(-H_{gg}/RT)$ (see, e.g. Drolet and Galibois, 1971; Simpson and Aust, 1972; Evans et al., 2001). At face value, the observed size evolution of recrystallized grains is in fair agreement with predictions based on equation (2) using Karato's (1989) experimentally derived parameters $m = 2$, $k_{gg,0} = 1.6\cdot10^{-8}\,m^2\,s^{-1}$, and $H_{gg} = 160\,kJ\,mol^{-1}$ (Fig. 5c).

When data are available for 16 and 70 h long annealing stages at a given temperature, the difference in grain size is however small (Fig. 5c). In conventional grain growth experiments such a plateau would indicate an effect of the starting grain size. The

calculation of critical nucleus size indicated much smaller values, though, suggesting that starting grain size can be neglected in Eq. (2) for new grains. This reasoning may not apply to the recrystallized host fragments, though. Two alternative explanations deserve consideration. Firstly, the apparent initial stagnation in grain size can simply be an effect of the convolution between the resolution limit of the EBSD analysis and the true grain size distribution (indeed the majority of distributions decreases monotonically as expected for this type of resolution issue). The peaks of the distributions come close to or exceed the limit of resolution only for extended annealing at high temperature. For short durations and/or low temperature only the tail of the distributions is sampled. Secondly, continuous nucleation would also lead to an initial absence of growth since the distribution functions would be continuously reloaded at their small-size end. Yet, we consider a significant continuous nucleation rate during annealing unlikely, because the "nuclei" in this type of recrystallization phenomena are actually formed during the deformation stage.

5.3 Kinetics of static recrystallization

Recrystallization from the deformed microstructure resembles a phase transformation (here the replacement of deformed material by grains with smaller dislocation density) involving overlapping and concurrent processes of nucleation, growth and impingement. Transformation kinetics is frequently modeled relying on the so-called Johnson-Mehl-Avrami-Kolmogorov (JMAK) equation (e.g. Johnson and Mehl, 1939; Christian, 2002, Liu et al., 2004). Below we firstly apply previously presented versions of the JMAK equation to our data before deriving an extended version that accounts for the time dependence of the driving force for growth. The complexities of the spacial distribution of recrystallization features in heterogeneously deformed materials as the peridotite samples of this study cannot be accounted for in this modeling.

5.3.1 Conventional Avrami-analysis

For site saturation or continuous nucleation and isothermal conditions, the formation of new grains can be modeled by the conventional JMAK-kinetics equation

$$X_V(t) = X_A(t) = 1 - \exp\left[-(k_{\text{trans}}t)^n\right] \tag{3}$$

5 where $X_V(t)$ and $X_A(t)$ denote transformed volume and area fractions, t time, and n is typically called the Avrami-exponent. The exponent depends on the dimensionality of growth and the rate-controlling process (e.g. interface vs. volume diffusion). Parameter k_{trans} is a rate constant assumed to have an Arrhenius-type temperature dependence, i.e. $k_{\text{trans}} = k_{\text{trans},0}\exp(-Q_{\text{trans}}/RT)$ with an effective activation energy Q_{trans} that is not

10 an activation enthalpy of a single atomistic process but reflects nucleation and growth processes. At face value, our data suggest an Avrami-exponent close to 1 at least for extended annealing (Fig. 6) and an effective activation energy of $\sim 150\,\text{kJ}\,\text{mol}^{-1}$ rather independent of the temperature at which the deformation took place preceding the annealing stage.

15 An Avrami-exponent as low as 1 is at odds with the microstructural observation that growth of grains occurs rather randomly in three dimensions. Spacial distribution of severely damaged material may reduce the dimensionality of growth to some extent but the very width and volume of the highly damaged zones clearly exceeds that of quasi-one-dimensional features. Such growth geometry is associated with $n = 3$ and 4

20 for site saturation and continuous nucleation, respectively. Exponents also depend on the process that controls the transfer of atoms from deformed grains to recrystallized grains (interface kinetics vs. diffusion kinetics) but we suppose that the growth of recrystallized grains is diffusion controlled. Recent modifications of the JMAK-equation considered complex nucleation scenarios (Kempen et al., 2002; Liu et al., 2004) and

25 yield time dependent exponents and activation energies. We however consider that an unlikely source for the low exponents observed here (see discussion on nucleation above) and follow a different path of extending the JMAK-approach by accounting for the time dependence of the driving force for growth.

Title Page

Abstract | Introduction

Conclusions | References

Tables | Figures

|◄ | ►|

◄ | ►

Back | Close

Full Screen / Esc

Printer-friendly Version

Interactive Discussion

5.3.2 Extension of Avrami-analysis for time dependent growth rate

We consider the situation that all nuclei are already formed before the heat treatment started but account for the time dependence of the growth rate of nuclei $\dot{G}$, or their boundary velocity $v(t) = \dot{G}$. Then, the transformed volume fraction evolves according to

$$X_V(t) = 1 - \exp\left[-fN\left(\int_0^t v(\tau)d\tau\right)^3\right] \qquad (4)$$

where f denotes a shape factor and N the number of nuclei present (see also Luo, 2012). The exponent of 3 represents three-dimensional growth. For simplicity we consider isotropic growth of spherical particles, i.e. $f = 4\pi/3$. The positive argument of the exponential function in (4) represents the extended volume ratio, i.e. $X_V(t) = 1 - \exp\left(-X^{\text{ext}}\right)$ with $X^{\text{ext}} = V^{\text{ext}}/V$.

In the context of static recrystallization of deformed materials, the driving force for grain boundary migration is the difference in dislocation density of the growing nuclei and their environment, the deformed material. We may assume that the dislocation density of the growing nuclei remains negligible during progressing annealing since static annealing excludes further deformation. Thus, the current dislocation density $\rho(t)$ (note, for the sake of presentational simplicity we drop the index "rec" for the size of recrystallites and the index "def" for the dislocation density of deformed material used in Eq. (1) in the following) of the relics of deformed material determines the driving force (reduction in free energy due to consumption of dislocations by moving grain boundaries, i.e. $F = \Delta G$)

$$F(t) \simeq -\frac{\gamma}{d(t)} + \mu b^2 \rho(t). \qquad (5)$$

New grains have to evolve above the minimum relation for a positive driving force of their growth, i.e. $F(t) > -\gamma/d_{\text{min}} + \mu b^2 \rho(t)$ allowing us to introduce $F(t) = \chi\mu b^2 \rho(t)$ with

Title Page

Abstract | Introduction

Conclusions | References

Tables | Figures

|◄ | ►|

◄ | ►

Back | Close

Full Screen / Esc

Printer-friendly Version

Interactive Discussion

$\chi > 0$. Here, we further rely on the standard linear relation between velocity and driving force (e.g. Ballufi et al., 2005)

$$v(t) = m_{gb}F(t) \simeq \chi m_{gb}\mu b^2\rho(t) \tag{6}$$

in which the mobility $m_{gb} = \Omega D/\delta RT$ (with molar volume Ω, grain boundary diffusion coefficient $D = D_0\exp(-H_{gg}/RT)$, and grain boundary width δ) assuming that the kinetics of boundary migration can be described by an intrinsic boundary mobility independent of the actual driving force. Vandermeer et al. (1997) explicitly showed for copper that the grain boundary mobility does not differ for curvature-driven growth and strain-induced growth.

The next step in our derivation of transformation kinetics is to specify the reduction in dislocation density with time due to recovery. Typically, the rate of change in dislocation density is proportional to some positive power of dislocation density (e.g. annihilation requires encounters of dislocations, the number of encounters is the higher the higher their density; see for example Nes, 1995; Liu and Evans, 1997)

$$\dot\rho \propto \rho^p. \tag{7}$$

For first ($p = 1$) and second ($p = 2$) order reaction kinetics, integration yields specifically

$$\rho(t) = \rho_0 \begin{cases} \exp(-Bt) & \text{for } p = 1 \\ \frac{1}{1+K\rho_0 t} & \text{for } p = 2, \end{cases} \tag{8}$$

when choosing $t_0 = 0$ for convenience. The two reaction constants reflect the intrinsic activation of the rate-controlling recovery process, i.e. $B = B_0\exp(-H_\rho/RT)$ and $K =$

$K_0 \exp(-H_\rho/RT)$. The relative extended volume calculates as

$$X^{\text{ext}} = \frac{V_{\text{trans}}^{\text{ext}}}{V} = \frac{4}{3}\pi \frac{N}{V}\left(\chi m_{\text{gb}}\mu b^2\right)^3 \rho_0^3 \begin{cases} \left(\int_0^t \exp(-B\tau)\,\mathrm{d}\tau\right)^3 & \text{for } p = 1 \\ \left(\int_0^t \frac{\mathrm{d}\tau}{1+K\rho_0\tau}\right)^3 & \text{for } p = 2 \end{cases} \qquad (9)$$

and upon integration one finds the transformation to proceed according to

$$X_V(t) = 1 - \begin{cases} \exp\left\{-\frac{A\rho_0^3}{B^3}\left[1 - \exp(-Bt)\right]^3\right\} & \text{for } p = 1 \\ \exp\left\{-\frac{A}{K^3}\left[\ln(1 + K\rho_0 t)\right]^3\right\} & \text{for } p = 2 \end{cases} \qquad (10)$$

5   where we introduced $A = 4\pi\eta(\chi m_{\text{gb}}\mu b^2)^3/3$ with the nucleus density $\eta = N/V$.

In contrast to the classical JMAK theory the extended volume may reach a limit of

$$\lim_{t\to\infty} X_V(t) = 1 - \begin{cases} \exp\left\{-\frac{A\rho_0^3}{B^3}\right\} & \text{for } p = 1 \\ \exp\left\{-\frac{A}{K^3}\right\} & \text{for } p = 2 \end{cases} \qquad (11)$$

when the driving force is lost due to recovery before the recrystallization came to completion (Fig. 14). Substantial recrystallization occurs in a rather limited window of about
10   one order of magnitude in dimensionless time. The associated characteristic recrystallization time is $t_{\text{rec}} \sim 1/A^{1/3}\rho_0$ for first and second order kinetics. In the range of measurable percentages (1 to 100 %), Eq. (10) either represent standard JMAK time dependence with a power of 3 leading to completion of recrystallization or lower and time-dependent exponents and stagnation of recrystallization before completion.

Title Page

Abstract | Introduction

Conclusions | References

Tables | Figures

◄ | ►

◄ | ►

Back | Close

Full Screen / Esc

Printer-friendly Version

Interactive Discussion

The effective Avrami parameters can be determined according to

$$n' = \frac{d}{d \ln t} \ln \left[\ln \left(\frac{1}{1 - X_V(t)} \right) \right] \text{ and}$$

$$Q' = -R \frac{d}{d(1/T)} \ln \left[\ln \left(\frac{1}{1 - X_V(t)} \right) \right]. \tag{12}$$

After algebraic manipulation, we find the exponent as

$$n' = \begin{cases} \frac{3Bt}{\exp(Bt) - 1} & \text{for } p = 1 \\ \frac{3}{\ln(1 + K\rho_0 t)} \frac{K\rho_0 t}{1 + K\rho_0 t} & \text{for } p = 2 \end{cases} \tag{13}$$

and the activation energy as

$$Q' = 3H_{gg} + (n' - 3)H_\rho \text{ for } p = 1, 2 \tag{14}$$

assuming that the temperature dependence of the diffusion coefficient, i.e. $D \propto \exp(-H_{gg}/RT)$ dominates the temperature dependence of the grain boundary mobility m_{gb}. Initially, the change in growth rate is negligible and thus the classic Avrami parameters, an effective exponent of 3 and an effective activation energy of $3H_{gg}$, are found. With increasing time recovery becomes rate-relevant. The effective exponent decreases from 3 to 0, for either order but second order kinetics yields a very slow decrease towards the end of the recrystallization process (Fig. 15a). The effective activation energy is ultimately given by the difference $3(H_{gg} - H_\rho)$ (Fig. 15a). Thus, even for a very simple nucleation scenario as considered here (site saturation), effective Avrami parameters can be significantly time dependent when the driving force for growth exhibits a temporal evolution. Thus, small Avrami exponents do not necessarily indicate a low dimensionality of growth. Effective activation energies are not easily interpreted either, owing to the two fundamental thermally activated processes that contribute to the kinetics of recrystallization, boundary migration and recovery.

Deformation and recrystallization of olivine

C. A. Trepmann et al.

Title Page

Abstract	Introduction
Conclusions	References
Tables	Figures

|◄ ►|

◄ ►

Back Close

Full Screen / Esc

Printer-friendly Version

Interactive Discussion

5.4 Quantitative analysis

Thanks to the large number of studies on various aspects of the kinetics of deformation and recovery processes operative in olivine aggregates one can actually attempt a quantitative analysis of the extended Avrami equation presented above. Instead of performing a numerical parameter search by an inversion procedure or the like, we rather investigate the basic relations among the involved model parameters and their general capability of modeling our observations. This strategy is motivated by the significant non-linearity of the multi-parameter problem. The questions that we want to answer are which requirements are posed on the involved kinetics parameters for the basic observations to be in accord with model predictions and whether these requirements are compatible with currently available constraints on the involved parameters.

The basic observation that we consider is the combined occurrence of effective Avrami parameters, $n' \sim 1$ and $Q' \sim 150 \pm 50\,\mathrm{kJ\,mol^{-1}}$, at recrystallized volume fractions of $X_V \sim 1$. We do face the issue here that volume ratios should probably be calculated relative to a volume representing deformed material rather than the entire sample volume but the distinction of reference is of subordinate relevance for our order of magnitude analysis. Solving $X_V(t_{0.1}) = 0.1$ according to Eq. (10) for the time $t_{0.1}$ at which 10 % recrystallization is reached and then analyzing $n'(t_{0.1})$ gives the following approximate constraints on the involved kinetics parameters:

$$\frac{B}{A^{1/3}\rho_0} \simeq 0.84 \left[\ln\left(\frac{1}{0.9}\right) \right]^{1/3} \simeq 1.8 \text{ for } p = 1 \text{and} \tag{15}$$

$$\frac{K}{A^{1/3}} \simeq 2.8 \left[\ln\left(\frac{1}{0.9}\right) \right]^{1/3} \simeq 6.0 \text{ for } p = 2. \tag{16}$$

Furthermore, the effective activation energy provides a constraint on the relation between the activation enthalpies of grain boundary migration and recovery for $n' \sim 1$,

Full Screen / Esc

Printer-friendly Version

Interactive Discussion

$$150 \, \text{kJ} \, \text{mol}^{-1} \sim 3H_{gg} - 2H_\rho. \tag{17}$$

Finally, we require that for the investigated temperature range recrystallization actually occurs on laboratory time scales, i.e. the characteristic time of transformation ought to be

$$t_{rec} = \frac{1}{A^{1/3}\rho_0} \sim 10^{5\pm1} \, \text{s} \tag{18}$$

for first and second order kinetics.

The time of occurrence of recrystallization provides a direct constraint on the order of magnitude of grain-boundary mobility, i.e. $m_{gb} \sim 3.4 \times 10^{-19\pm1} \, \text{m}^4 \, \text{J}^{-1} \, \text{s}^{-1}/\chi$. This estimate seems to range at the lower end of (or actually falls short of) previously reported values for grain-boundary mobility (Fig. 16a). Yet, apart from uncertainties in the estimates of nucleus density and initial dislocation density (lower than assumed values in either of the two lead to larger values in predicted grain-boundary mobility), driving-force parameter χ as well as grain-boundary energy γ play crucial roles in this comparison. Experimentally determined grain-growth constants have to be converted to mobility using a geometrical constant as well as grain-boundary energy, i.e. $m_{gb} = k_{gg}/8\gamma$. In particular the early phases of the recrystallization process may involve subgrains with interfacial energies orders of magnitude smaller than the assumed value of $1 \, \text{J} \, \text{m}^{-2}$ valid for large-angle grain boundaries. The mobility would be correspondingly larger.

Various constraints on grain boundary mobility in olivine aggregates are available. We focus on the grain growth law reported by Karato (1989), the range of mobility presented in the review by Evans et al. (2001), and a recent quantitative estimate derived from analyzing piezometric relations of olivine aggregates (Hackl and Renner, 2013). For the temperature range of our experiments a spread of 10^{-18} to $10^{-11} \, \text{m}^4 \, \text{J}^{-1} \, \text{s}^{-1}$ is indicated (Fig. 16a). The corresponding activation enthalpies are $\sim 160 \, \text{kJ} \, \text{mol}^{-1}$ and $335 \, \text{kJ} \, \text{mol}^{-1}$ from Karato (1989) and Hackl and Renner (2013), respectively. The latter

is actually not a result of the analysis by Hackl and Renner (2013) but chosen relying on the consistency between diffusion creep rates and diffusion coefficients for Si-diffusion along grain boundaries in ol-aggregates (see Hirth and Kohlstedt, 2003). Toriumi (1982) reported $210 \pm 20\,\mathrm{kJ\,mol^{-1}}$ for grain boundary migration at isostatic stress

5 conditions. The lack of quantitative consistency among the various constraints on grain boundary mobility likely stems from the involvement of pores that pin the boundaries. Considering experimental uncertainties and the uncertainties in transformation steps between the different measured parameters, it is thus fair to conclude that using the extended Avrami model with currently available constraints on grain boundary mobility

10 does not lead to a conflict with the observed transformation kinetics.

Insertion of relation (18) into (15) and (16) yields constraints on the recovery kinetics

$$B \simeq 1.78 \cdot 10^{-5 \mp 1}\,\mathrm{s^{-1}}\ \text{for}\ p = 1 \tag{19}$$

$$K \simeq \frac{6.0 \cdot 10^{-5 \mp 1}\,\mathrm{s^{-1}}}{\rho_0} \sim 6.0 \cdot 10^{-20 \mp 1}\,\mathrm{m^2\,s^{-1}}\ \text{for}\ p = 2. \tag{20}$$

15 The experimental studies on the recovery kinetics of olivine crystals unanimously find recovery to follow second order kinetics (i.e. $p = 2$ in Eqs. 9 to 16). The rate constants reported recently by Farla et al. (2011) deviate from earlier studies (Kohlstedt et al., 1980; Karato and Ogawa, 1982; Karato et al., 1993) by about two orders of magnitude at the conditions of the actual experiments performed to investigate the kinetics. Due

20 to the difference in activation enthalpy this difference is diminished at the conditions of our experiments (Fig. 16b). The various studies yield a fairly consistent range for activation enthalpy of about 240 to $355\,\mathrm{kJ\,mol^{-1}}$ that may however be extended due to experimental uncertainties. These values are markedly lower than the value for diffusion of Si in olivine of $530\,\mathrm{kJ\,mol^{-1}}$ (Dohmen et al., 2002), relevant if dislocation climb

25 was rate-controlling for the recovery processes (Karato et al., 1993). The requirement expressed by Eq. (19) falls right onto the experimentally derived parameters (Fig. 16b).

The constraint on effective activation energy (17) can be matched with a range of combinations of activation enthalpies (Fig. 17). Thus, the activation enthalpy relation

Title Page

Abstract | Introduction

Conclusions | References

Tables | Figures

|◀ | ▶|

◀ | ▶

Back | Close

Full Screen / Esc

Printer-friendly Version

Interactive Discussion

does not provide an overly diagnostic means of identifying the likely relevant set of kinetics parameters. From an analysis of the literature values, we chose three pairs of enthalpies H_{gg} and H_{ρ} as representative for further analyses. The effect of pressure differences among the various studies is subordinate compared to the quoted experimental uncertainties ($11\,cm^3\,mol^{-1}$ reported for recovery (Kohlstedt et al., 1980) for example corresponds to a change of 11 to $22\,kJ\,mol^{-1}$ from ambient pressure to 1 or 2 GPa, respectively).

In summary, the constraints (15) to (18) for a match between our experimental observations and the proposed extended Avrami model can all be met in consistency with currently available quantitative estimates on the involved kinetics parameters. Out of the range of possible parameters we picked three sets and performed a forward calculation of the characteristics of the recrystallization progress (Fig. 18). According to the extended Avrami model, recrystallization in our experiments is characterized by effective parameters n' and Q' that vary quite significantly with time.

5.5 Implications

5.5.1 Extrapolation to natural conditions

The above introduced recrystallization model is now extrapolated to 600 °C. A temperature of 600 °C likely represents the lower base of the seismogenic zone for the oceanic lithosphere, as seismological studies found that the occurrence of earthquakes in the oceanic lithosphere appear to be limited in depth-range by the 600 °C isotherm (Abercrombie and Ekström, 2001, 2003; McKenzie et al., 2005). Consistently, evidence from naturally and experimentally deformed peridotite was presented that the transition from brittle to plastic deformation occurs at about 600 °C (e.g. Jaroslow et al., 1996; Warren and Hirth, 2006; Boettcher et al., 2007; Druiventak et al., 2011).

Depending on the pair of activation enthalpies used, significant recrystallization will occur after tens to hundreds of years or it may last up to ten thousands of years until volume fractions of detectable size have undergone this specific microstructural

Title Page

Abstract | Introduction

Conclusions | References

Tables | Figures

|◀ | ▶|

◀ | ▶

Back | Close

Full Screen / Esc

Printer-friendly Version

Interactive Discussion

transformation. The set of lowest enthalpies gives the shortest duration since extrapolating them from experimental conditions causes the least change of the characteristic recrystallization times (tens of hours in the laboratory). Recovery kinetics has a modest effect on only one of the three considered scenarios of activation enthalpies (pair (1) in

5 Figs. 17 and 19) for which also the fastest recrystallization is predicted. The other two scenarios essentially exhibit growth limited recrystallization as indicated by the steep slope corresponding to $n' = 3$ almost to the end and actually reaching completion.

For the more rapid transformations, the concept of static recovery may become erroneous since stresses may possibly not fully relax on such short time scales but recrys-

10 tallization will occur during creep with decreasing rate. The microfabrics found after our "kick and creep" experiments (core-and-mantle like microstructure with a large range in recrystallized sizes and a weak to absent CPO not depending on the stress field) qualitatively show the same characteristics as the ones found after "kick and cook" experiments performed at the same temperature for the same duration. Quantitatively,

15 the average size of recrystallized grains seems unaffected by the superposed creep, yet the recrystallized area is larger for dynamic recrystallization than for static recrystallization, probably caused by additional grain size reduction during early stages of creep.

Apart from the uncertainties in the used kinetics parameters, the extrapolation of

20 our model may suffer from unresolved nucleation kinetics. While we argued against thermally activated nucleation we cannot exclude that early site saturation is a simplification that does not fully hold for natural conditions. Accounting for more complex nucleation scenarios as well as varying temperatures requires sophisticated numerical modeling (e.g. Kaminski and Ribe, 2001).

25 The presented extrapolation replaces our previous zero order attempt of using the effective activation energy of recrystallization of $150 \pm 50\,\mathrm{kJ\,mol^{-1}}$ to estimate the time reduction of our experiments in comparison to natural conditions (see Druiventak et al., 2012). Since two basic thermally activated processes, growth and recovery that are linked rather than independent, control recrystallization the effective activation energy

Title Page

Abstract | Introduction

Conclusions | References

Tables | Figures

|◄ | ►|

◄ | ►

Back | Close

Full Screen / Esc

Printer-friendly Version

Interactive Discussion

Deformation and recrystallization of olivine

C. A. Trepmann et al.

cannot be used for extrapolation but a detailed model that accounts for the link between the processes has to be employed. The extended model predicts, however, a dominance of the thermal activation of grain boundary migration, i.e. again a single activation enthalpy rather than a time and temperature dependent effective activation
5 energy control recrystallization progress at temperatures of 600 °C or lower. Therefore, the previous prediction and the current extrapolation coincide for the pair of activation enthalpies for which H_{gg} almost coincides with Q'. This parameter set predicts the shortest characteristic times for recrystallization (tens of years) while the other two predict time scales that are larger by about one or more orders of magnitude.

10 **5.5.2 Diagnostic microstructures**

The most characteristic microstructural features after our "kick and cook" and "kick and creep" experiments are:

1. the high range in recrystallised grain size within one sample, where former highly damaged zones are still traceable by zones with relative finer grain sizes ($< 10\,\mu m$)
15   compared to areas beyond the highly damaged zones, even after annealing at high temperature (≥ 900 °C) and long isostatic annealing times (≥ 69 h).

2. Also the observed absence of a CPO that can be related to the axes of the strain field (almost random CPO for new grains and host control for recrystallized fragments) will remain stable in a prolonged low stress environment.

20   The recrystallized area reached in samples from "kick and creep" experiments is larger than the one reached in "kick and cook" by about a factor of two. Yet, the observation of similar grain sizes, grain size distributions and orientation characteristics of recrystallized grains suggests that minor creep during relaxing stresses does not affect the microstructural identification potential of the characteristic sequence of high-stress
25 deformation followed by recrystallisation at decreasing stresses. Our experiments show that strain localization during initial high-stress low-temperature plasticity controls the

Title Page

Abstract | Introduction

Conclusions | References

Tables | Figures

|◄ | ►|

◄ | ►

Back | Close

Full Screen / Esc

Printer-friendly Version

Interactive Discussion

recrystallization microstructure (grain size distribution and CPO) developed at isostatic or low stress conditions, leading to a modification and preservation of the initial heterogeneities. Thus, the combination of a large range in recrystallized grain size and a CPO that is not related to the strain field are characteristics that allow recognizing a high-
5 stress event in natural rocks even considering minor creep during stress relaxation and a prolonged thermal history at low stresses.

5.5.3 Reloading

In nature, the reloading of seismically active faults may be relevant. The stress resolution in our "kick-cook-kick" and "cook-kick" experiments is probably not sufficient to
10 assess the strength during the second deformation in great detail. The value of these experiments lies in their microstructural record. The microstructures found after annealing of the undeformed natural material that was then deformed at high stresses and low temperature ("cook and kick") do not show any difference to the microstructures found when the peridotite is deformed right the way ("kick"). The microstructures found af-
15 ter "kick-cook-kick" indicate that deformation will continue to alter the porphyroclasts, preferentially those in contact with recrystallized areas (Fig. 12c, d). Strain localization during the second "kick" seems to be controlled by pre-existing inhomogeneities and local stress concentration, e.g. at the contacts between fine-grained and coarse grained areas behaving differently during low-temperature plasticity, the rheology dom-
20 inating deformation regime during high-stress deformation (Druiventak et al., 2011). Thus, repeated stress cycles (seismic events) presumably increase the recrystallized volume.

6 Summary and conclusions

During isostatic annealing of our "kick and cook" experiments, initiation of recrystalliza-
25 tion is associated with (a) "new grains" replacing deformed crystalline material within

highly-damaged zones, i.e. characterized by a high density of tangled dislocations and cell structures, and (b) host fragments with inherited dislocation density, termed "recrystallized host fragments". The local density of new grains is controlled by the local strain accumulated by low-temperature plasticity and microfracturing during the "kick"
5 experiment, leading to localized fine-grained aggregates of recrystallized grains tracing former highly damaged zones. At annealing temperatures ≥ 900 °C and times ≥ 69 h, the highly damaged zones are completely replaced by recrystallized grains. After replacement of the highly damaged zones boundaries between defect-free new grains are solely controlled by interfacial energy, pinning of boundaries by voids partially ham-
10 pers further growth. In contrast, strain-induced migration of boundaries between new grains and host fragments with inherited defect-density can further proceed due to gradients in stored strain energy, explaining that at higher temperatures and annealing times recrystallisation area exceeds the area of the original highly damaged zones. The differences in grain boundary migration in aggregates of defect-free new grains
15 and host fragments with inherited dislocation density cause a characteristic range in recrystallized grain size in samples from experiments at high annealing temperatures (≥ 900 °C) and times (≥ 69 h). Former highly damaged zones are traceable by zones with relative finer grain sizes (< 10 μm) even after annealing at high temperature (up to 1100 °C) and long annealing time (up to 144 h) as well as in our "kick and creep"
20 experiments. Thus, a high-stress (coseismic deformation) event is likely detectable in shear zone peridotites even after a prolonged thermal low-stress history with or without creep (postseismic creep) by a large range in grain sizes with localized fine-grained aggregates and weak to absent CPO that is not interpretable in terms of intracrystalline glide systems. When deforming an annealed rock volume again rapidly at high stresses
25 ("kick-cook-kick"), then strain is apparently concentrated in porphyroclasts surrounded by recrystallized grains, suggesting that repeated high-stress (seismic) events continuously increase the recrystallized volume. Extrapolation of an extended Avrami-kinetics equation for which parameters were constrained from our results and previously reported kinetics parameters suggests that the time-dependent transformation

(i.e. replacement of deformed material by formation of new defect-poor grains) leading to the characteristic microstructure may develop in as little as some tens of years and not more than ten thousands of years at about 600 °C, i.e. the base of the seismogenic zone. The characteristic heterogeneous microstructures are likely sufficiently stable to serve as an indicator of past seismic activity after a prolonged thermal low-stress history with minor creep and finally exhumation.

References

Abercrombie, R. E. and Ekström, G.: Earthquake slip on oceanic transform faults, Nature, 410, 74–77, 2001.

Abercrombie, R. E. and Ekström, G.: A reassessment of the rupture characteristics of oceanic transform earthquakes, J. Geophys. Res., 108, 2225, doi:10.1029/2001JB000814, 2003.

Atkinson, H. V.: Overview no. 65: theories of normal grain growth in pure single phase systems, Acta Metall. Mater., 36, 469–491, 1988.

Avrami, M.: Kinetics of phase change. I General theory, J. Chem. Phys., 7, 1103–1112, 1939.

Avrami, M.: Kinetics of phase change. II Transformation-time relations for random distribution of nuclei, J. Chem. Phys., 8, 212–224, 1940.

Avrami, M.: Granulation, phase change, and microstructure kinetics of phase change. III, J. Chem. Phys., 9, 177–184, 1941.

Ben-Zion, Y.: Collective behavior of earthquakes and faults: continuum-discrete transitions, progressive evolutionary changes, and different dynamic regimes, Rev. Geophys., 46, RG4006, doi:10.1029/2008RG000260, 2008.

Ben-Zion, Y. and Lyakhovsky, V.: Analysis of aftershocks in a lithospheric model with seismogenic zone governed by damage rheology, Geophys. J. Int., 165, 197–210, 2006.

Birtel, S. and Stöckhert, B.: Quartz veins record earthquake-related brittle failure and short term ductile flow in the deep crust, Tectonophysics, 457, 53–63, 2008.

Boettcher, M. S., Hirth, G., and Evans, B.: Olivine friction at the base of oceanic seismogenic zones, J. Geophys. Res., 112, B01205, doi:10.1029/2006JB004301, 2007.

Chopra, P. N. and Paterson, M. S.: The experimental deformation of dunite, Tectonophysics, 78, 453–473, 1981.

Christian, J. W.: The Theory of Transformations in Metals and Alloys: Part I+ II, Elsevier Science Ltd, Oxford, 2002.

5 Cooper, R. F. and Kohlstedt, D. L.: Interfacial energies in the olivine-basalt system, Adv. Earth Planet. Sci., 12, 217–228, 1982.

Deer, W. A., Howie, R. A., and Zussman, J.: An Introduction to the Rock-Forming Minerals, Longman, Essex, 1992.

Dessa, J. X., Klingelhoefer, F., Graindorge, D., André, C., Permana, H., Gutscher, M. A.,
10 Chauhan, A., and Singh, S. C.: Megathrust earthquakes can nucleate in the forearc mantle: evidence from the 2004 Sumatra event, Geology, 37, doi:10.1130/G25653A, 2009.

Dohmen, R., Chakraborty, S., and Becker, H. W.: Si and O diffusion in olivine and implications for characterizing plastic flow in the mantle, Geophys. Res. Lett., 29, 2030, doi:10.1029/2002GL015480, 2002.

15 Drolet, J. and Galibois, A.: Altering the time cycle of heat treatment by preannealing prior to grain growth, Metall. Mater. Trans. B, 2, 53–64, 1971.

Druiventak, A., Trepmann, C. A., Renner, J., and Hanke, K.: Low-temperature plasticity of olivine during high stress deformation of peridotite at lithospheric conditions – an experimental study, Earth Planet. Sc. Lett., 311, 199–211, 2011.

20 Druiventak, A., Matysiak, A., Renner, J., and Trepmann, C. A.: Kick-and-cook experiments on peridotite: simulating coseismic deformation and post-seismic creep, Terra Nova, 24, 62–69, 2012.

Drury, M. R. and Urai, J. L.: Deformation-related recrystallization processes, Tectonophysics, 172, 235–253, 1990.

25 Durinck, J., Devincre, B., Kubin, L., and Cordier, P.: Modeling the plastic deformation of olivine by dislocation dynamics simulations, Am. Mineral., 92, 1346–1357, 2007.

Duyster, J. and Stöckhert, B.: Grain boundary energies in olivine derived from natural microstructures, Contrib. Mineral. Petr., 140, 567–576, 2001.

Ellis, S. and Stöckhert, B.: Elevated stresses and creep rates beneath the brittle-ductile
30 transition caused by seismic faulting in the upper crust, J. Geophys. Res, 109, B05407, doi:10.1029/2003JB002744, 2004.

Evans, B. E., Renner, J. R., and Hirth, G. H.: A few remarks on the kinetics of static grain growth in rocks, Int. J. Earth Sci., 90, 88–103, 2001.

Deformation and recrystallization of olivine

C. A. Trepmann et al.

Title Page

Abstract	Introduction
Conclusions	References
Tables	Figures

◀◀   ▶▶

◀   ▶

Back   Close

Full Screen / Esc

Printer-friendly Version

Interactive Discussion

Farla, R., Kokkonen, H., Fitz Gerald, J., Barnhoorn, A., Faul, U., and Jackson, I.: Dislocation recovery in fine-grained polycrystalline olivine, Phys. Chem. Miner., 38, 363–377, 2011.

Fitz Gerald, J. D. and Stünitz, H.: Deformation of granitoids at low metamorphic grade. I: Reactions and grain size reduction, Tectonophysics, 221, 269–297, 1993.

Hackl, K. and Renner, J.: High-temperature deformation and recrystallization: a variational analysis and its application to olivine aggregates, J. Geophys. Res.-Sol. Ea., in press, 2013.

Hirth, G. and Kohlstedt, D.: Rheology of the upper mantle and the mantle wedge: a view from the experimentalists, in: Inside the Subduction Factory, edited by: Eiler, J., Geophysical Monograph, AGU, Washington, 83–105, 2003.

Holyoke III, C. W. and Kronenberg, A. K.: Accurate differential stress measurement using the molten salt cell and solid salt assemblies in the Griggs apparatus with applications to strength, piezometers and rheology, Tectonophysics, 494, 17–31, 2010.

Humphreys, F. J. and Hatherly, M.: Recrystallization and Related Annealing Phenomena, 2nd edn., Elsevier Ltd, Oxford, 605 pp., 2004.

Jackson, I., Fitz Gerald, J. D., Faul, U. H., and Tan, B. H.: Grain-size-sensitive seismic wave attenuation in polycrystalline olivine, J. Geophys. Res.-Sol. Ea., 107, 2360, doi:10.1029/2001JB001225, 2002.

Jaroslow, G. E., Hirth, G., and Dick, H. J. B.: Abyssal peridotite mylonites: implications for grain-size sensitive flow and strain localization in the oceanic lithosphere, Tectonophysics, 256, 17–37, 1996.

Johnson, W. A. and Mehl, R. F.: Reaction kinetics in processes of nucleation and growth, T. Am. Inst. Min. Met. Eng., 135, 416–458, 1939.

Kaminski, É. and Ribe, N. M.: A kinematic model for recrystallization and texture development in olivine polycrystals, Earth Planet. Sc. Lett., 189, 253–267, 2001.

Karato, S.-I.: Grain growth kinetics in olivine aggregates, Tectonophysics, 168, 255–273, 1989.

Karato, S.-I. and Ogawa, M.: High-pressure recovery of olivine: implications for creep mechanisms and creep activation volume, Phys. Earth Planet. In., 28, 102–117, 1982.

Karato, S.-I., Rubie, D. C., and Yan, H.: Dislocation recovery in olivine under deep upper mantle conditions: implications for creep and diffusion, J. Geophys. Res., 98, 9761–9768, 1993.

Kempen, A. T. W., Sommer, F., and Mittemeijer, E. J.: The isothermal and isochronal kinetics of the crystallisation of bulk amorphous Pd40Cu30P20Ni10, Acta Mater., 50, 1319–1329, 2002.

Deformation and recrystallization of olivine

C. A. Trepmann et al.

Title Page

Abstract | Introduction

Conclusions | References

Tables | Figures

Back | Close

Full Screen / Esc

Printer-friendly Version

Interactive Discussion

Kohlstedt, D. L., Nichols, H. P. K., and Hornack, P.: The effect of pressure on the rate of dislocation recovery in olivine, J. Geophys. Res., 85, 3122–3130, 1980.

Küster, M. and Stöckhert, B.: High differential stress and sublithostatic pore fluid pressure in the ductile regime – microstructural evidence for short-term post-seismic creep in the Sesia Zone, Western Alps, Tectonophysics, 303, 263–277, 1999.

Liu, M. and Evans, B.: Dislocation recovery kinetics in single-crystal calcite, J. Geophys. Res., 102, 24801–24809, 1997.

Liu, F., Sommer, F., and Mittemeijer, E. J.: An analytical model for isothermal and isochronal transformation kinetics, J. Mater. Sci., 39, 1621–1634, 2004.

Luo, H.: Effect of concurrent recovery on Avrami exponent of the softening kinetics after hot deformation, Mater. Sci. Eng. A-Struct., 532, 44–49, 2012.

Matysiak, A. K. and Trepmann, C. A.: Crystal-plastic deformation and recrystallization of peridotite controlled by the seismic cycle, Tectonophysics, 530–531, 111–127, 2012.

McKenzie, D., Jackson, J., and Priestley, K.: Thermal structure of oceanic and continental lithosphere, Earth Planet. Sc. Lett., 233, 337–349, 2005.

Moghadam, R. H., Trepmann, C. A., Stöckhert, B., and Renner, J.: Rheology of synthetic omphacite aggregates at high pressure and high temperature, J. Petrol., 51, 921–945, 2010.

Nes, E.: Recovery revisited, Acta Metall. Mater., 43, 2189–2207, 1995.

Nicolas, A. and Poirier, J. P.: Crystalline Plasticity and Solid State Flow in Metamorphic Rocks, John Wiley, New York, 444 pp., 1976.

Nüchter, J.-A. and Ellis, S.: Complex states of stress during the normal faulting seismic cycle: role of midcrustal postseismic creep, J. Geophys. Res., 115, B12411, doi:10.1029/2010JB007557, 2010.

Nüchter, J.-A. and Stöckhert, B.: Vein quartz microfabrics indicating progressive evolution of fractures into cavities during postseismic creep in the middle crust, J. Struct. Geol., 29, 1445–1462, 2007.

Passchier, C. W. and Trouw, R. A. J.: Microtectonics, 2nd edn., Springer Verlag, Berlin-Heidelberg-New York, 2008.

Platt, J. P. and Behr, W. M.: Grainsize evolution in ductile shear zones: implications for strain localization and the strength of the lithosphere, J. Struct. Geol., 33, 537–550, 2011a.

Platt, J. P. and Behr, W. M.: Lithospheric shear zones as constant stress experiments, Geology, 39, 127–130, 2011b.

Deformation and recrystallization of olivine

C. A. Trepmann et al.

Title Page

Abstract	Introduction
Conclusions	References
Tables	Figures

◄ | ►

◄ | ►

Back | Close

Full Screen / Esc

Printer-friendly Version

Interactive Discussion

Renner, J., Zerbian, A., and Stöckhert, B.: Microstructures of synthetic polycrystalline coesite aggregates. The effect of pressure, temperature, and time, Lithos, 41, 169–184, 1997.

Rolandone, F., Bürgmann, R., and Nadeau, R. M.: The evolution of the seismic-aseismic transition during the earthquake cycle: constraints from the time-dependent depth distribution of aftershocks, Geophys. Res. Lett., 31, L23610, doi:10.1029/2004GL021379, 2004.

Rybacki, E., Renner, J., Konrad, K., Harbott, W., Rummel, F., and Stöckhert, B.: A servohydraulically-controlled deformation apparatus for rock deformation under conditions of ultra-high pressure metamorphism, Pure Appl. Geophys., 152, 579–606, 1998.

Schaff, D. P., Bokelmann, G. H. R., Beroza, G. C., Waldhauser, F., and Ellsworth, W. L.: High-resolution image of Calaveras Fault seismicity, J. Geophys. Res.-Sol. Ea., 107, 2186, doi:10.1029/2001JB000633, 2002.

Scholz, C. H.: The mechanics of earthquakes and faulting, 2nd edn., Cambridge University press, Cambridge, 2002.

Shimizu, I.: Stress and temperature dependence of recrystallized grain size: a subgrain misorientation model, Geophys. Res. Lett., 25, 4237–4240, 1998.

Sibson, R. H.: Transient discontinuities in ductile shear zones, J. Struct. Geol., 2, 165–171, 1980.

Simpson, C. J., and Aust, K. T.: Grain boundary migration, Surf. Sci., 31, 479–497, 1972.

Singh, S. C., Carton, H., Tapponnier, P., Hananto, N. D., Chauhan, A. P. S., Hartoyo, D., Bayly, M., Moeljopranoto, S., Bunting, T., and Christie, P.: Seismic evidence for broken oceanic crust in the 2004 Sumatra earthquake epicentral region, Nat. Geosci., 1, 777–781, 2008.

Stipp, M. and Kunze, K.: Dynamic recrystallization near the brittle-plastic transition in naturally and experimentally deformed quartz aggregates, Tectonophysics, 448, 77–97, 2008.

Stünitz, H., Fitz Gerald, J. D., and Tullis, J.: Dislocation generation, slip systems, and dynamic recrystallization in experimentally deformed plagioclase single crystals, Tectonophysics, 372, 215–233, 2003.

Toriumi, M.: Grain boundary migration in olivine at atmospheric pressure, Phys. Earth Planet. In., 30, 26–35, 1982.

Toriumi, M. and Karato, S.-I.: Experimental studies on the recovery process of deformed olivines and the mechanical state of the upper mantle, Tectonophysics, 49, 79–95, 1978.

Trepmann, C. and Stöckhert, B.: Mechanical twinning of jadeite – an indication of synseismic loading beneath the brittle-plastic transition, Int. J. Earth Sci., 90, 4–13, 2001.

Title Page

Abstract | Introduction

Conclusions | References

Tables | Figures

◀ | ▶

◀ | ▶

Back | Close

Full Screen / Esc

Printer-friendly Version

Interactive Discussion

Trepmann, C. A. and Stöckhert, B.: Cataclastic deformation of garnet: a record of synseismic loading and postseismic creep, J. Struct. Geol., 24, 1845–1856, 2002.

Trepmann, C. A. and Stöckhert, B.: Quartz microstructures developed during non-steady state plastic flow at rapidly decaying stress and strain rate, J. Struct. Geol., 25, 2035–2051, 2003.

5 Trepmann, C. A., Stöckhert, B., Dorner, D., Moghadam, R. H., Küster, M., and Röller, K.: Simulating coseismic deformation of quartz in the middle crust and fabric evolution during postseismic stress relaxation – an experimental study, Tectonophysics, 442, 83–104, 2007.

Vandermeer, R. A., Jensen, D. J., and Woldt, E.: Grain boundary mobility during recrystallization of copper, Metall. Mater. Trans. A, 28, 749–754, 1997.

10 Warren, J. M. and Hirth, G.: Grain size sensitive deformation mechanisms in naturally deformed peridotites, Earth Planet. Sci. Lett., 248, 438–450, 2006.

Deformation and recrystallization of olivine

C. A. Trepmann et al.

Title Page

Abstract	Introduction
Conclusions	References
Tables	Figures

◀ ▶

◀ ▶

Back Close

Full Screen / Esc

Printer-friendly Version

Interactive Discussion

5, 463–524, 2013

Table 1. Mechanical data from the deformation and annealing experiments.

sample#	High-stress deformation ("kick") $p_c = 1$ GPa					Quasi-static annealing ("cook") $p_c = 2$ GPa							
	$T_{c,def}$ [°C]	$T_{m,def}$ [°C]	SR [10^{-5} s^{-1}]	$\Delta\sigma_{max}$ [GPa]	ε_{max} [%]	$T_{c,ann}$ [°C]	$T_{m,ann}$ [°C]	t_{ann} [h]	A [%]	d_{exp} [μm]	std [μm]	d_{max} [μm]	ε_{tot} [%]
KH17[1]	260	326	3.0	1.6	25								nd
B9016	301	296	7.4	1.4	28								33
B9027	301	298	6.6	1.1	19								24
B9001[1,2]	601	614	7.9	1.1	19			no annealing					6
B9003	602	614	8.0	1.1	21								nd
B9009[1,2]	601	595	7.6	1.3	24								26
B9030	602	584	7.4	1.1	16								17
B9021	301	307	7.5	1.2	25	702	704	16.4	0.2	2.9	0.9	6.3	25
B9034	301	285	6.7	0.9	18	702	667	144.3	1.0	4.0	1.6	9.9	28
B9020	301	279	6.9	1.6	23	801	764	16.6	1.2	3.6	1.0	7.0	21
B9019	301	303	7.4	1.3	23	901	890	16.8	2.6	3.8	1.2	8.0	15
B9018	301	337	7.4	1.3	25	1001	858	16.2	5.1	3.9	1.5	11.6	30
B9017	301	300	7.4	1.4	27	1001	1011	69.2	12.6	5.2	2.7	23.1	25
B9028	301	298	7.0	1.6	22	1001	992	144.0	30.9	9.9	4.9	31.7	14
B9007[2]	602	nd	8.0	1.0	18	702	nd	16.2	0.2	3.1	0.9	6.4	11
B9031	601	610	7.3	1.0	14	702	705	144.1	1.2	3.4	1.5	9.7	23
B9005[2]	601	592	8.1	1.0	17	801	790	16.3	0.5	3.4	1.3	10.0	18
B9035	601	601	8.0	1.0	21	801	787	72.2	1.5	3.1	1.4	11.9	26
B9024	601	577	7.6	1.3	19	801	768	144.0	1.2	4.1	1.6	10.7	14
B9004[2]	601	622	7.5	1.0	17	901	929	16.2	2.7	3.0	1.4	11.0	9
B9022	601	613	8.2	0.9	23	901	831	69.0	2.9	3.0	1.2	10.0	31
B9025	601	599	7.8	1.5	20	901	895	144.0	6.0	4.0	2.1	18.0	27
B9006[2]	601	625	7.7	1.2	18	1001	1018	16.2	9.3	4.0	2.2	18.0	11
B9010	602	496	8.0	1.3	23	1001	1007	68.9	7.5	4.0	3.1	41.0	5
B9029	602	579	7.9	1.0	19	1001	961	143.9	18.7	5.0	3.5	26.0	29
B9036	601	618	7.9	1.0	15	1100	1089	69.3	26.7	5.0	5.1	42.0	26
B9026			no deformation			1000	1002	68.8	0.3	4.2	3.6	25.8	3
B9032[p]			no deformation			1001	nd	75.2	< 0.1	4.9	3.5	40.8	1

$T_{c,def}$, $T_{m,def}$, $T_{c,ann}$ and $T_{m,ann}$: temperature readings (not corrected for pressure) of the controlling and monitoring thermocouples during deformation and annealing, respectively.
SR: strain rate; $\Delta\sigma_{max}$: maximum differential stress; ε_{true}: sum of elastic and inelastic strain derived from stress-strain curves; t_{ann}: annealing-time; A: area covered by recrystallized grains; d_{exp}, std and d_{max}: expectation value, standard deviation and maximum grain size of the diameter of recrystallised olivine grains; ε_{tot}: total strain determined from sample shortening after quenching.
[p] Experiment performed in a piston cylinder apparatus.
[1] Druiventak et al. (2011).
[2] Druiventak et al. (2012).
nd: not determined

SED
5, 463–524, 2013

Deformation and recrystallization of olivine

C. A. Trepmann et al.

Title Page

Abstract | Introduction
Conclusions | References
Tables | Figures

|◄ | ►|
◄ | ►
Back | Close

Full Screen / Esc

Printer-friendly Version

Interactive Discussion

Table 2. Mechanical data of experiments of "kick and creep" (a) and "kick-cook-kick" (b) experiments.

(a)

sample#	High-stress deformation ("kick") p_c = 1 GPa					Low-stress deformation at high temperature ("creep") p_c = 2 GPa										
	$T_{c,def}$ [°C]	$T_{m,def}$ [°C]	SR [10^{-5} s^{-1}]	$\Delta\sigma_{max}$ [GPa]	ε_{max} [%]	$T_{c,ann}$ [°C]	$T_{m,ann}$ [°C]	t_{ann} [h]	A [%]	d_{exp} [µm]	std [µm]	d_{max} [µm]	SR [s^{-1}]	$\Delta\sigma$ [GPa]	$\varepsilon_{tot} - \varepsilon_{max}$ [%]	ε_{tot} [%]
B9037	301	309	6.6	1.1	17	1001	1005	70.2	25.6	5.7	2.9	22.0	4×10^{-7}	0.30	10	27
B9038	301	326	7.0	1.5	21	1001	Nd	70.8	nd	6.4	5.4	29.5	1×10^{-6}	0.44	19	50
B9039	602	629	7.7	1.0	17	1001	955	69.8	23.6	nd	nd	nd	6×10^{-7}	0.39	16	33

(b)

sample#	First deformation ("kick") p_c = 1 GPa (except B9015: 2.0 GPa)					Quasi-isostatic annealing ("cook") p_c = 2 GPa							Second deformation ("kick") p_c = 1 GPa (except B9015: 2 GPa)						
	$T_{c,def}$ [°C]	$T_{m,def}$ [°C]	SR [10^{-5} s^{-1}]	$\Delta\sigma_{max}$ [GPa]	$\varepsilon_{max\,1}$ [%]	$T_{c,ann}$ [°C]	$T_{m,ann}$ [°C]	t_{ann} [h]	A [%]	d_{exp} [µm]	std [µm]	d_{max} [µm]	$T_{c,def}$ [°C]	$T_{m,def}$ [°C]	SR [10^{-5} s^{-1}]	$\Delta\sigma_{max}$ [GPa]	$\varepsilon_{max\,2}$ [%]	$\varepsilon_{tot} - \varepsilon_{max\,1}$ [%]	ε_{tot} [%]
B9040	301	302	7.3	1.26	23	1001	nd	69.1	30.2	4.5	3.8	22.0	301	311	2.42	nd	16	11	34
B9014	602	nd	7.6	1.17	25	1001	nd	16.5	15.9	3.6	1.9	28.4	602	nd	5.81	2.0	9	12	37
B9015	601	592	7.6	1.29	18	1001	nd	16.6	20.0	4.9	3.7	23.5	602	nd	4.94	2.0	9	18	36
B9043	602	nd	7.4	1.27	19	1001	nd	69.0	nd	nd	nd	nd	601	nd	5.28	2.1	11	20	39
B9044	no deformation					1001	971	69.9	nd	nd	nd	nd	601	570	8.34	2.1	15	11	11

Notation for table heads as for Table 1; numbers quoted in italic: strain rate and stress during creep estimated as described in the text.

Deformation and recrystallization of olivine

C. A. Trepmann et al.

Table 3. (a) Parameter estimates for the quantitative analysis of the extended Avrami model. (b) Constraints on activation enthalpies of involved processes.

a)	parameter	estimate	reference
	grain boundary energy γ	$1\,\mathrm{J\,m^{-2}}$	Cooper and Kohlstedt (1982); Duyster and Stöckhert (2001)
	shear modulus μ	$50\,\mathrm{GPa}$	Jackson et al. (2002)
	Burgers vector b	$0.6\,\mathrm{nm}$	Deer et al. (1992); Durinck et al. (2007)
	nucleus density $\eta = N/V$	$10^{18}\,\mathrm{m^{-3}}$	
	initial dislocation density of deformed material ρ_0	$10^{15}\,\mathrm{m^{-2}}$	
b)	process	activation enthalpy ($\mathrm{kJ\,mol^{-1}}$)	reference
	grain growth	$H_{gg} \sim 160\,\mathrm{kJ\,mol^{-1}}$ wet ($H_{gg} \sim 520\,\mathrm{kJ\,mol^{-1}}$ dry)	Karato (1989)
		$Q_{creep} \simeq H_{gbd}^{Si} \simeq H_{gg} = 335 \pm 75\,\mathrm{kJ\,mol^{-1}}$	Hirth & Kohlstedt (2003); Hackl & Renner (2013)
	grain boundary migration	$H_{gbm} \simeq 210 \pm 20\,\mathrm{kJ\,mol^{-1}}$	Toriumi (1982)
	recovery kinetics	$H_\rho = 300 \pm 15\,\mathrm{kJ\,mol^{-1}}$	Kohlstedt et al. (1980)
		$H_\rho = 460 \pm 42\,\mathrm{kJ\,mol^{-1}}$	Toriumi & Karato (1978)
		$H_\rho = 240 \pm 43\,\mathrm{kJ\,mol^{-1}}$ sol gel	Farla et al. (2011)
		$H_\rho = 355 \pm 81\,\mathrm{kJ\,mol^{-1}}$ SC ol	
	lattice diffusion of Si	$H_{ld}^{Si} = 529 \pm 41\,\mathrm{kJ\,mol^{-1}}$	Dohmen et al. (2002)

Title Page

Abstract | Introduction

Conclusions | References

Tables | Figures

|◀ | ▶|

◀ | ▶

Back | Close

Full Screen / Esc

Printer-friendly Version

Interactive Discussion
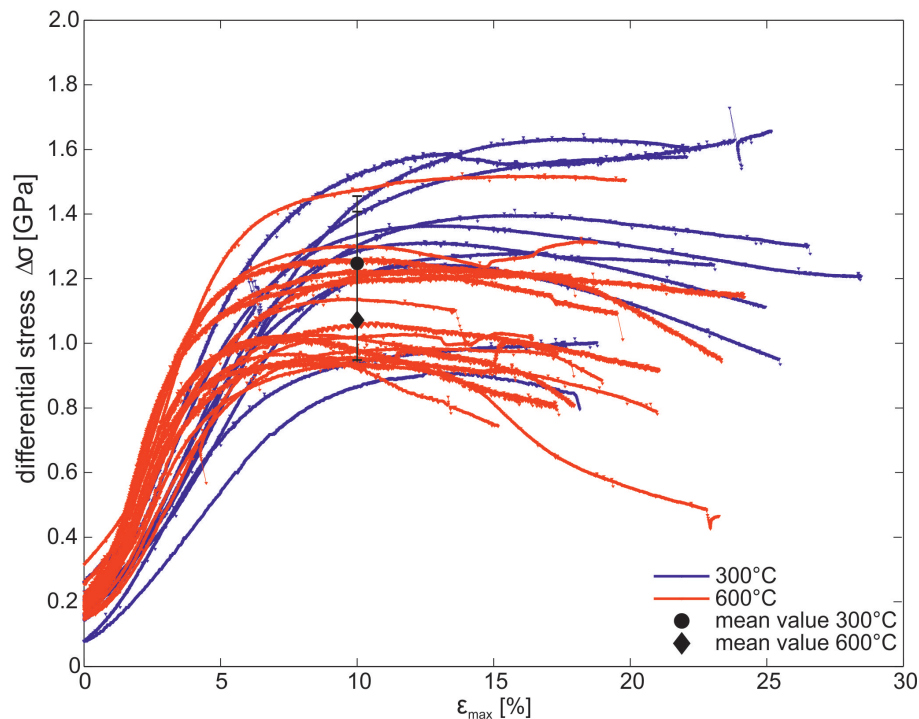
Fig. 1. Stress-strain curves for deformation at 300 °C and 600 °C. Mean value and standard deviation of stress at 10 % strain indicate a weak temperature dependence of strength.
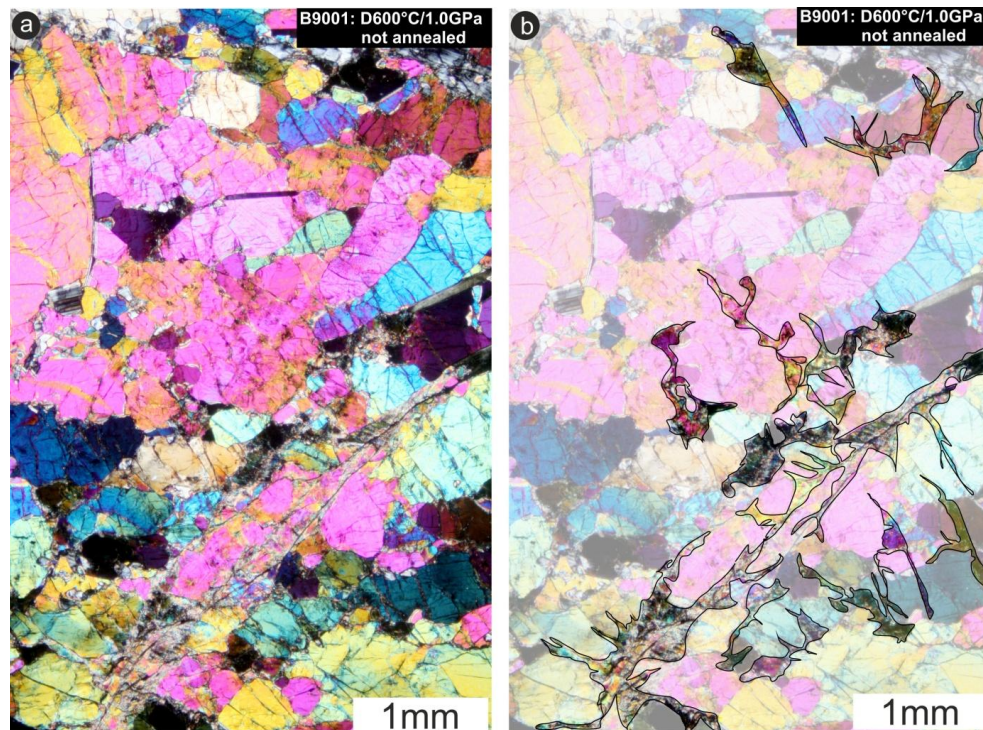
Fig. 2. (a, b) Optical micrograph (crossed polarizers) of sample B901 after deformation at 600 °C, 1 GPa that did not experience subsequent annealing. The yellow lines in **(b)** encircle the highly damaged zones, identified by optical microscopy (in combination with EBSD and TEM analyses).

Title Page

Abstract | Introduction

Conclusions | References

Tables | Figures

◄◄ | ►►

◄ | ►

Back | Close

Full Screen / Esc

Printer-friendly Version

Interactive Discussion
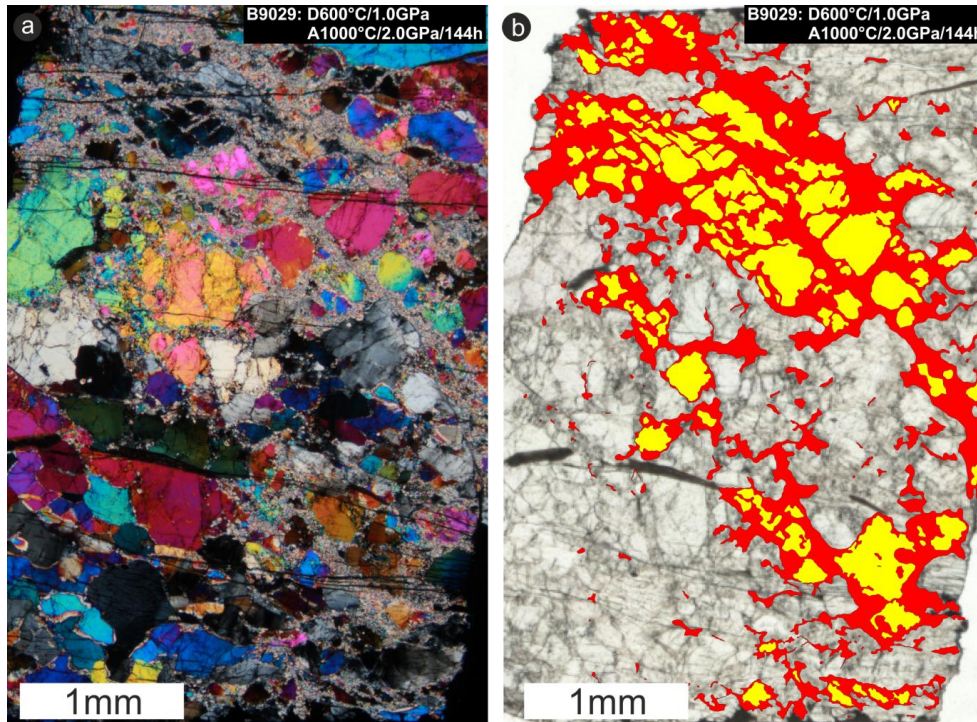
Fig. 3. (a) Optical micrograph (crossed polarizers) and **(b)** mapped recrystallised areas for sample B9029 deformed at 600 °C and annealed at 1000 °C for 144 h. The red color in **(b)** represents the recrystallised area and yellow represents olivine porphyroclasts surrounded by recrystallised olivine grains.

Title Page

Abstract | Introduction

Conclusions | References

Tables | Figures

|◄ | ►|

◄ | ►

Back | Close

Full Screen / Esc

Printer-friendly Version

Interactive Discussion
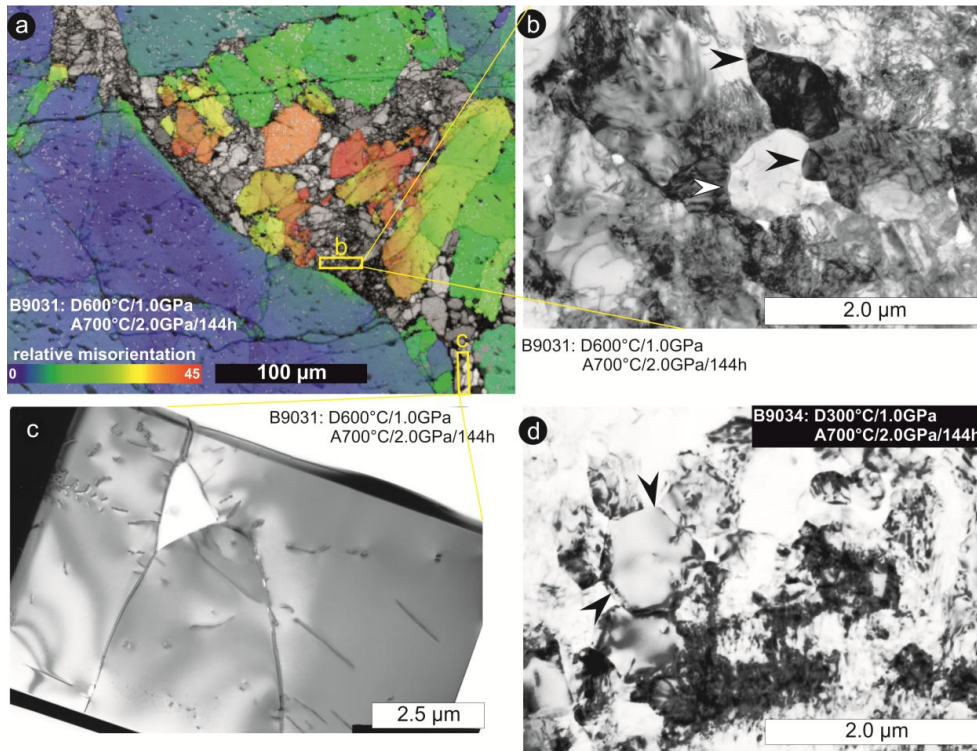
Fig. 4. (a) EBSD map with relative misorientation and **(b, c)** TEM micrographs of sample B9031, deformed at 600 °C and annealed at 700 °C for 144 h. **(d)** TEM micrograph of a sample B9034 deformed at 300 °C and annealed at 700 °C for 144 h. Note the "new grains", i.e. defect-poor crystallites (arrows in **(b, d)** in a distorted matrix of high defect density still present after annealing in zones of high strain generated during deformation. In contrast **(c)** shows a "recrystallized host fragment", see text for explanation.
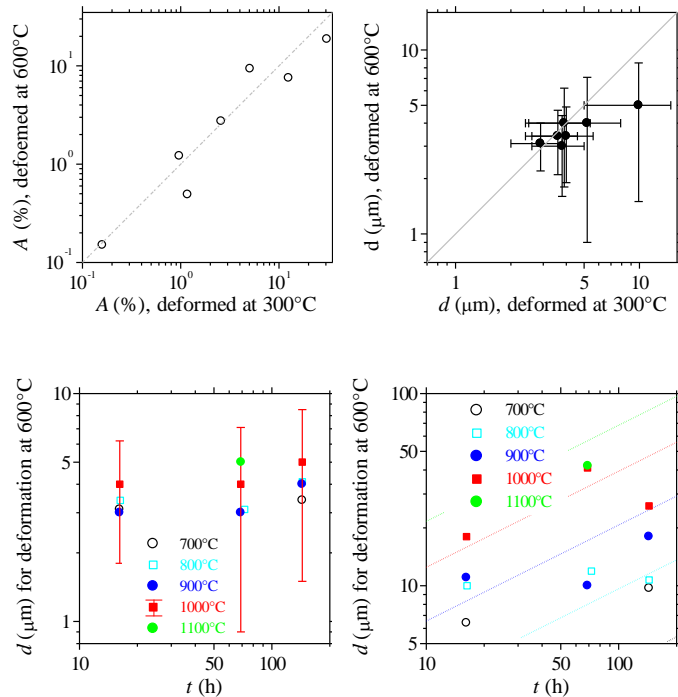
Fig. 5. Comparison of quantitative microstructure characteristics of annealing experiments following deformation at 300 °C and 600 °C: **(a)** recrystallized area and **(b)** average diameter of recrystallized grains. The error bars reflect the standard deviation. **(c)** Average grain size and **(d)** maximum grain size as a function of annealing time for indicated annealing temperatures. In **(c)** we present the standard deviation by error bars only for the data at 1000 °C for presentational clarity. Variability of results is comparable for all annealing temperatures (see Table 1). The dashed lines in **(d)** represent the empirical grain growth law after Karato (1980) with a starting grain size $d_0 = 0$.

Title Page

Abstract | Introduction

Conclusions | References

Tables | Figures

|◄ | ►|

◄ | ►

Back | Close

Full Screen / Esc

Printer-friendly Version

Interactive Discussion
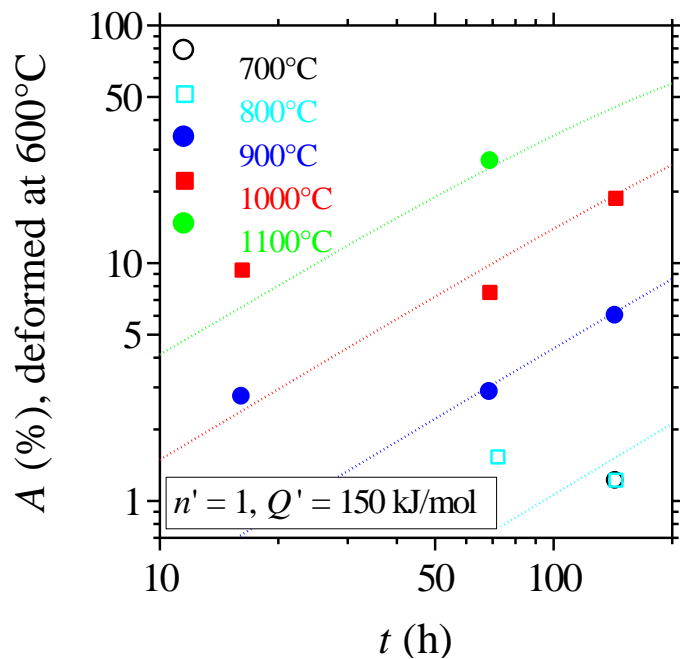
Fig. 6. Recrystallized area as a function of annealing time. The dashed lines indicate the predictions of the classical Avrami-kinetics Eq. (3) for the indicated effective exponent and effective activation energy. We restrict to representing results for samples deformed at 600 °C for presentational clarity. Similar findings hold for samples deformed at 300 °C.
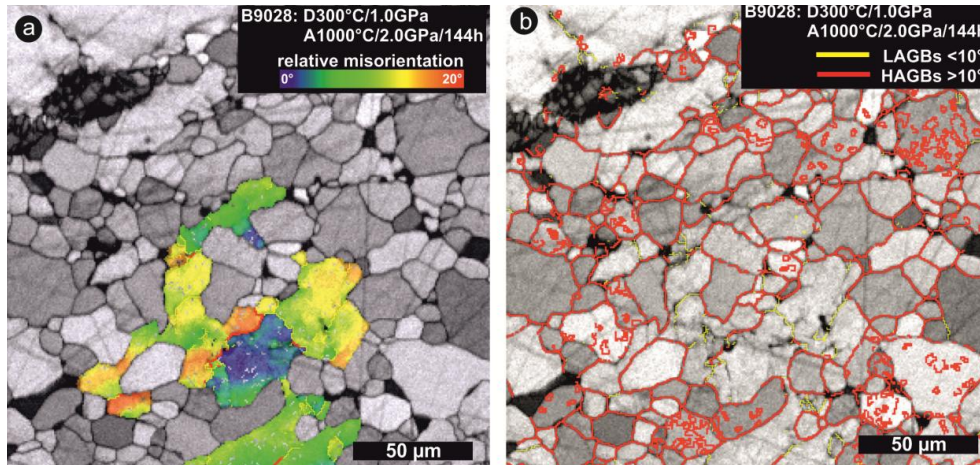
Fig. 7. EBSD map of sample B9028 deformed at 300 °C and annealed at 1000 °C for 144 h. **(a)** Highlighted is a host fragment recrystallised by strain-induced grain boundary migration characterized by its sutured grain boundaries and internal relative misorietation. **(b)** The same map, here with yellow lines indicating LAGBs and red lines indicating HAGBs. Note the contrast between the irregular shaped recrystallised host fragment and the isometric shape of new grains with smoothly curved HAGBs.
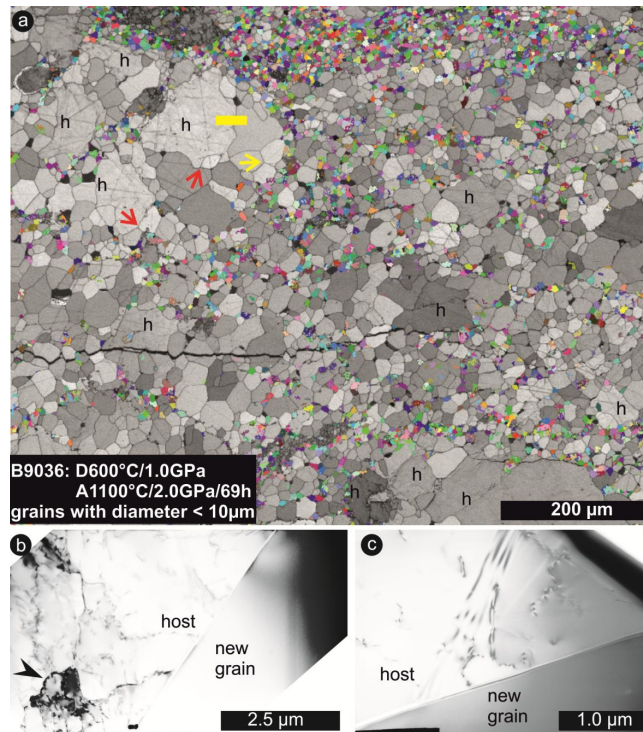
Fig. 8. (a) EBSD map shows grains with diameter < 10 µm in randomly selected colours in sample B09036 after deformation at 600 °C and annealing at 1100 °C for 69 h. Recrystallised host fragments (h) show sutured and concave grain boundaries. Note contrast to isometric shape of new grains with mostly convex boundaries. Yellow arrow marks equilibrium angle between boundaries where three new grains meet, in contrast to the boundaries to recrystallised host fragments (red arrows). Yellow bar marks location of FIB-prepared TEM sample of which micrographs are presented in **(b, c)**. **(b, c)** Recrystallised host fragment shows LAGBs and a moderate free dislocation density. The grain boundary between host and new grain is straight.
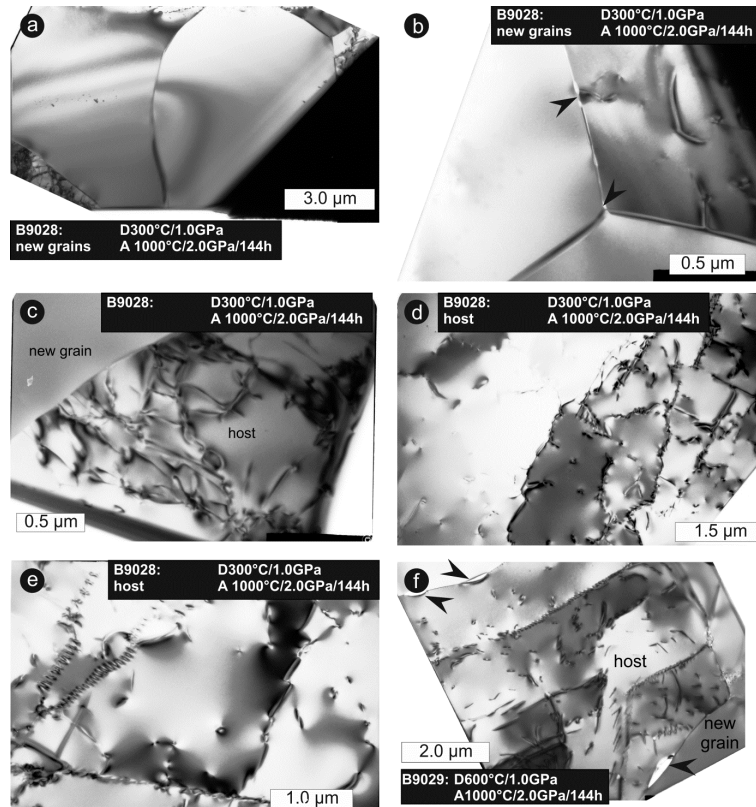
Fig. 9. TEM micrographs of sample B9028 deformed at 300 °C and annealed at 100 °C for 144 h **(a–e)** and of sample B9029 deformed at 600 °C and annealed at 1000 °C for 144 h **(f)**. TEM micrographs show defect-free new grains with smoothly curved boundaries to host crystals containing LAGBs and dislocations. Note voids along grain boundaries (arrows). At three-grain junctions the angle between the boundaries encloses 120°**(b)**.
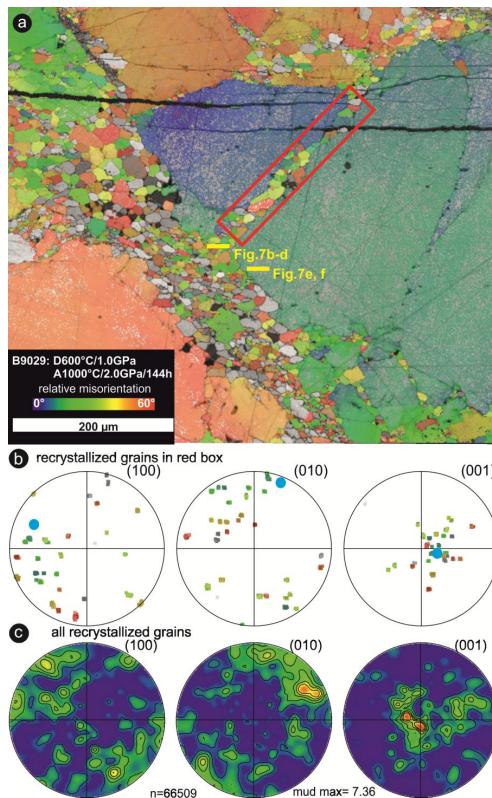
Fig. 10. (a) EBSD map showing recrystallised olivine grains in an intragranular zone and between two old grains after annealing at 1000 °C and 144 h. The yellow bars indicate the location of FIB-prepared TEM samples (Fig. 7a–e). The red rectangle indicates the area from which the crystallographic orientation is shown in the pole figures. **(b)** Pole figures displaying high misorientation angles between new grains (small dots) and host crystal (blue larger dot) in the intragranular zone (red rectangle). **(c)** Density plot of pole figures of all recrystallized grains in the map.

Title Page

Abstract | Introduction

Conclusions | References

Tables | Figures

|◀ | ▶|

◀ | ▶

Back | Close

Full Screen / Esc

Printer-friendly Version

Interactive Discussion
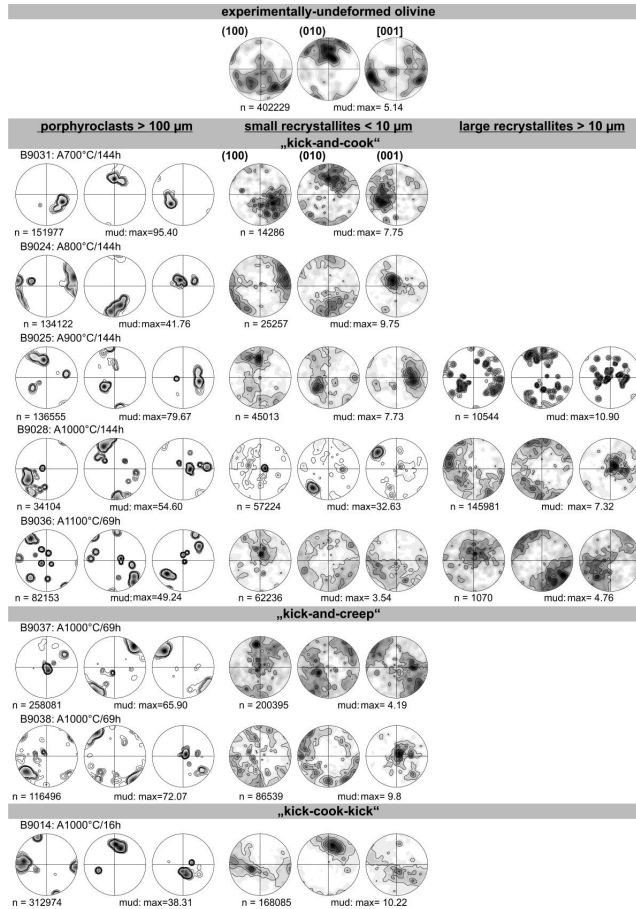
Fig. 11. Density plots of the crystallographic orientation of olivine crystals in an experimentally undeformed sample and in the deformed samples at the various experimental conditions, respectively (equal area projection, lower hemisphere).

Title Page

Abstract | Introduction

Conclusions | References

Tables | Figures

|◄ | ►|

◄ | ►

Back | Close

Full Screen / Esc

Printer-friendly Version

Interactive Discussion
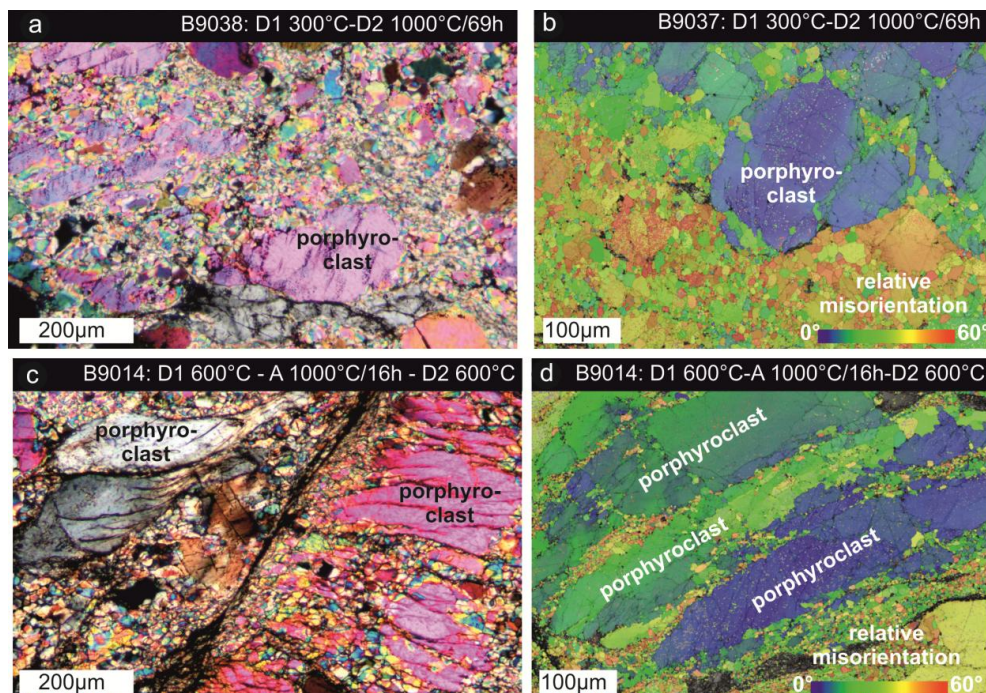
Fig. 12. (a) Optical micrograph (crossed polarizers) of sample B9038 and (b) EBSD map of sample B9037 both deformed at 300 °C and then deformed at 1000 °C at a low residual stress for ca. 69 h ("kick and creep" experiments). (c) Optical micrograph (crossed polarizers) and (d) EBSD map for sample B9014 after deformation at 600 °C at high stress, annealing at 1000 °C for 16 h and then again deformed at 600 °C at high stress ("kick-cook-kick" experiments).
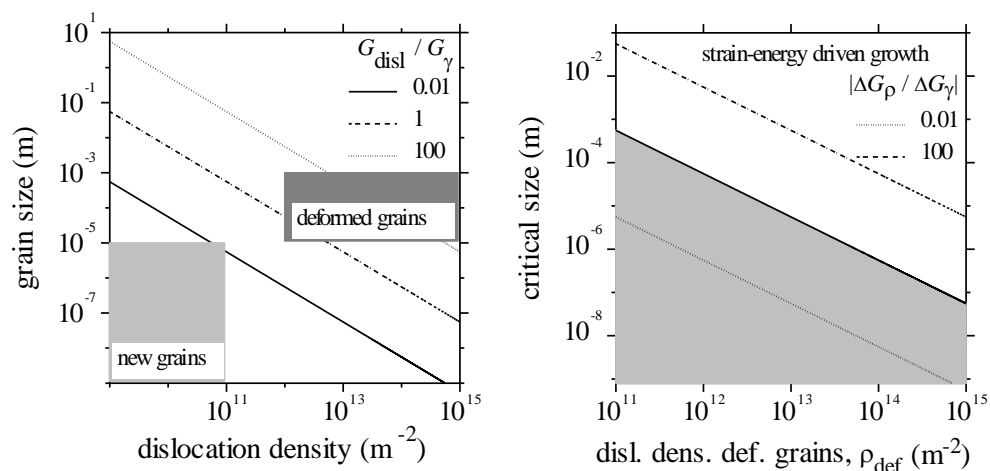
Fig. 13. (a) Relation between the free energies of new grains and deformed grains as determined by their size and their dislocation densities. **(b)** Critical size of grains for grain boundary migration in olivine (solid line, for example, a new grain needs a diameter of 1 μm in an environment with a dislocation density of $> 10^{14}\,\mathrm{m}^{-2}$ for strain-energy driven growth to occur). The dashed lines represent the indicated relations between the two contributions to free energy. The line for $\left|\Delta G_\rho / \Delta G_\gamma\right| = 0.01$ may also serve as an indication of the critical size relation for subgrains (index: sg) with $\gamma_{sg}/\gamma = 0.01$. Parameter estimates for olivine as given in Table 3. The lines of constant ratio between strain energy as represented by dislocation density and interfacial energy relation were calculated assuming that crystallites have much smaller size and dislocation density than the deformed grains as supported by the ranges highlighted in **(a)**.
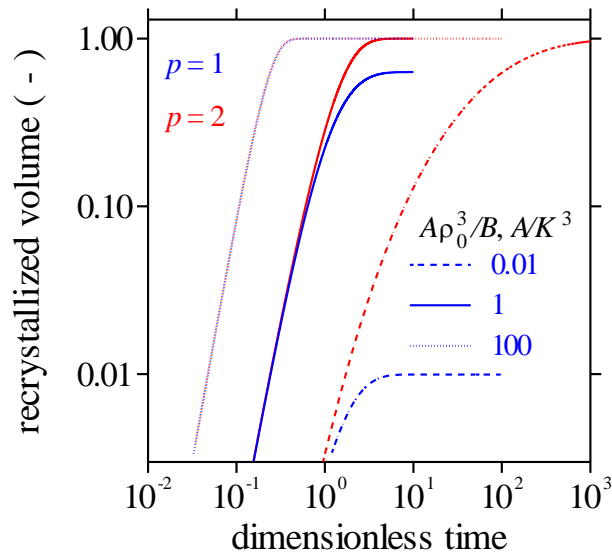
Fig. 14. Recrystallized volume according to Eq. (10) as a function of dimensionless time ($\hat{t}_{p=1} = Bt$ for $p = 1$ and $\hat{t}_{p=2} = K\rho_0 t$ for $p = 2$) in the range of "measurable" volume fractions. The ratios of kinetics constants $A\rho_0^3/B$ and A/K^3 have to be on order of 1 or less for recovery kinetics to affect the transformation progress.

Title Page

Abstract | Introduction

Conclusions | References

Tables | Figures

◄◄ | ►►

◄ | ►

Back | Close

Full Screen / Esc

Printer-friendly Version

Interactive Discussion
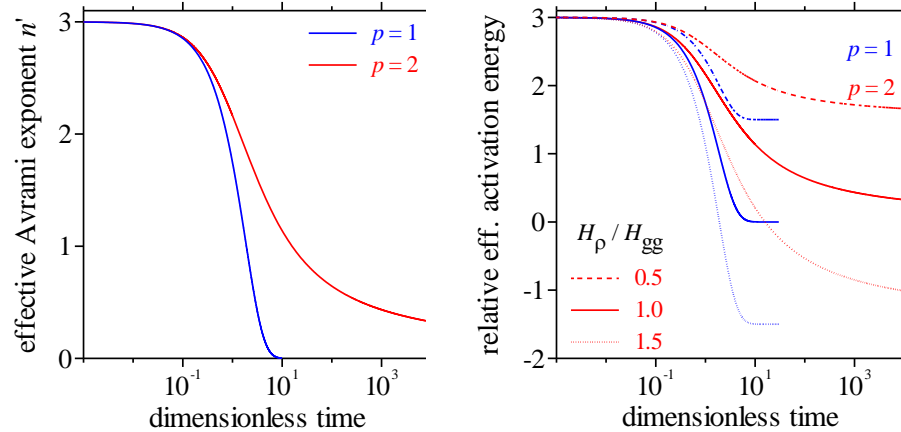
Fig. 15. (a) Effective Avrami exponent and **(b)** relative effective activation energy as a function of dimensionless time ($\hat{t}_{p=1} = Bt$ for $p = 1$ and $\hat{t}_{p=2} = K\rho_0 t$ for $p = 2$, see Eq. 10). For **(b)** Eq. (14) was divided by H_{gg} to arrive at relative values.
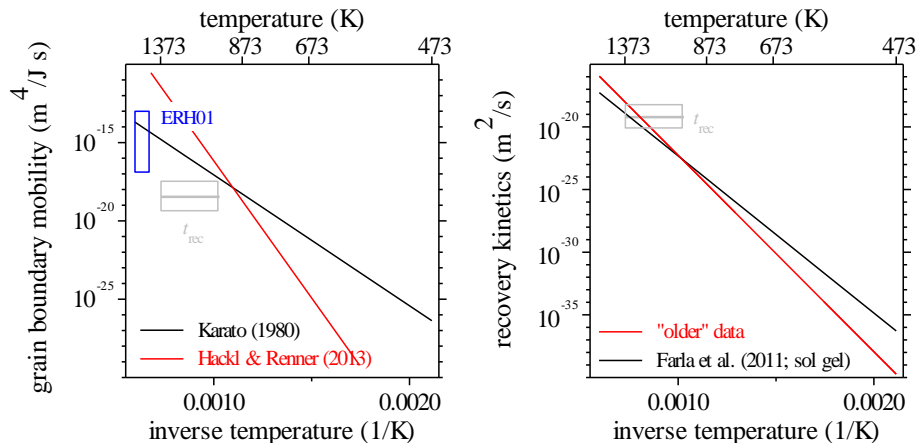
Fig. 16. Previously reported **(a)** grain boundary mobilities and **(b)** recovery kinetics parameters (for second order kinetics) in comparison to values required for the extended Avrami model to be in accord with observed recrystallization kinetics (boxes labeled, see text for details). The box labeled ERH01 represents the literature review by Evans et al. (2001). "Older" data refers to the collection of data that consistently deviate from Farla's et al. (2011) results.
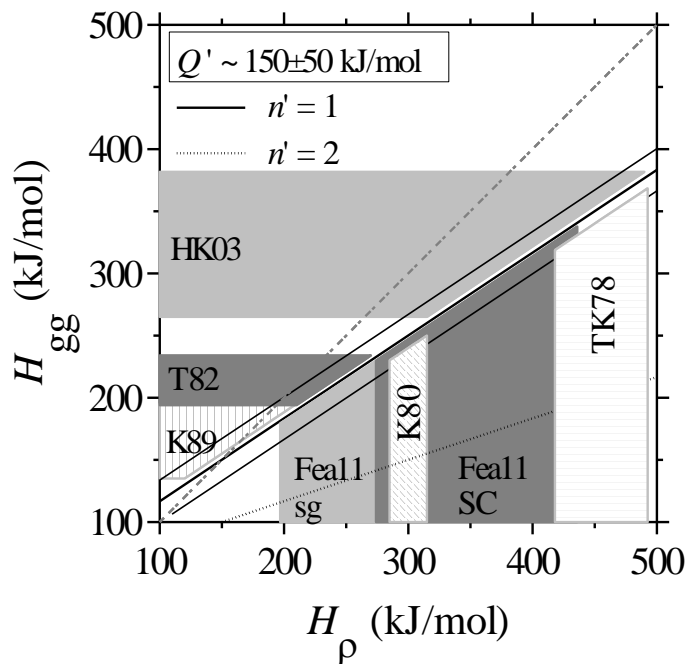
Fig. 17. Comparison of literature values for activation enthalpies of grain boundary mobility and dislocation recovery with the constraint provided by our experimental observations and the extended Avrami model (see Eq. 17). Consistency is for example found pairing for example the migration enthalpy by Toriumi (1982) [T82] and the recovery enthalpy found by Farla et al. (2011) [Fea11] for samples prepared from sol gel (sg). From the various possibilities we pick three pairs of H_{gg} and H_{ρ} values as representative: (185 kJ mol^{-1}, 200 kJ mol^{-1}); (230 kJ mol^{-1}, 270 kJ mol^{-1}); (335 kJ mol^{-1}, 428 kJ mol^{-1}). (K80: Karato, 1980; K89: Karato, 1989; HK02: Hirth and Kohlstedt, 2003; TK78: Toriumi and Karato, 1978).
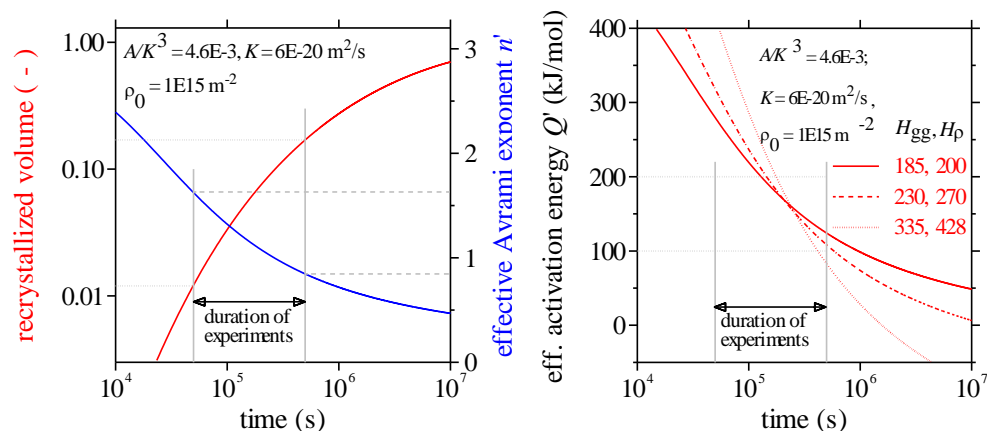
Fig. 18. (a) Recrystallization progress (left y-axis, red line) and effective Avrami exponent (right y-axis, blue line) and (b) effective activation energy as a function of time for second order recovery kinetics. The indicated values of the used kinetics parameters are derived on the basis of Eq. (15) to (18) and are in fair agreement with experimental constraints on them (see Figs. 16 and 17 and text for comprehensive discussion). The horizontal and vertical lines document how indeed recrystallized volume and effective Avrami exponent match our experimental observations in the range of relevant experimental duration. In (b) results for the three pairs of activation enthalpies are shown that were identified from the compilation of literature values in Fig. 17.
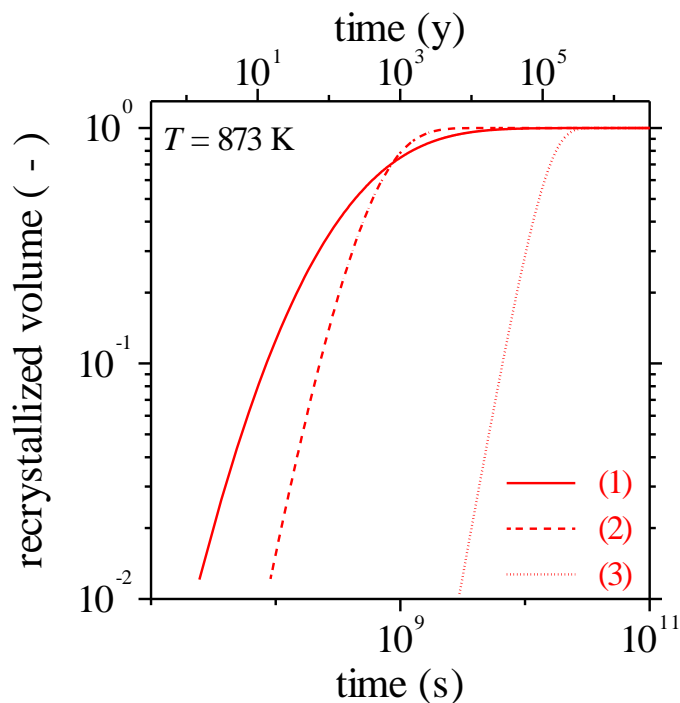
Fig. 19. Recrystallization progress extrapolated to 873 K for the three pairs of activation enthalpies identified from the compilation of literature values in Fig. 17:

1. $H_{gg} = 185 \, \mathrm{kJ\,mol^{-1}}, H_\rho = 200 \, \mathrm{kJ\,mol^{-1}}, A/K^3 = 2.3 \cdot 10^{-2}, K = 5.2 \cdot 10^{-23} \, \mathrm{m^2\,s^{-1}}$

2. $H_{gg} = 230 \, \mathrm{kJ\,mol^{-1}}, H_\rho = 270 \, \mathrm{kJ\,mol^{-1}}, A/K^3 = 3.2 \cdot 10^{-1}, K = 4.4 \cdot 10^{-24} \, \mathrm{m^2\,s^{-1}}$, and

3. $H_{gg} = 335 \, \mathrm{kJ\,mol^{-1}}, H_\rho = 428 \, \mathrm{kJ\,mol^{-1}}, A/K^3 = 8.7 \cdot 10^{1}, K = 1.7 \cdot 10^{-26} \, \mathrm{m^2\,s^{-1}}$.